

High-Performance Flexible Nanoscale Field-Effect Transistors Based on Transition Metal Dichalcogenides

Alwin Daus¹, Sam Vaziri¹, Victoria Chen¹, Cagil Koroglu¹, Ryan W. Grady¹, Connor S. Bailey¹, Hye Ryoung Lee², Kevin Brenner¹, Kirstin Schauble¹ and Eric Pop^{1,3,*}

¹Department of Electrical Engineering, Stanford University, Stanford, CA 94305, U.S.A.

²Geballe Laboratory for Advanced Materials, Stanford University, Stanford, CA 94305, U.S.A.

³Department of Materials Science & Engineering, Stanford University, Stanford, CA 94305, U.S.A.

*Corresponding author email: epop@stanford.edu

Two-dimensional (2D) semiconducting transition metal dichalcogenides (TMDs) are good candidates for high-performance flexible electronics. However, most demonstrations of such flexible field-effect transistors (FETs) to date have been on the micron scale, not benefitting from the short-channel advantages of 2D-TMDs. Here, we demonstrate flexible monolayer MoS₂ FETs with the shortest channels reported to date (down to 50 nm) and remarkably high on-current (up to 470 $\mu\text{A } \mu\text{m}^{-1}$ at 1 V drain-to-source voltage) which is comparable to flexible graphene or crystalline silicon FETs. This is achieved using a new transfer method wherein contacts are initially patterned on the rigid TMD growth substrate with nanoscale lithography, then coated with a polyimide (PI) film which becomes the flexible substrate after release, with the contacts and TMD. We also apply this transfer process to other TMDs, reporting the first flexible FETs with MoSe₂ and record on-current for flexible WSe₂ FETs. These achievements push 2D semiconductors closer to a technology for low-power and high-performance flexible electronics.

For several years, the “Internet-of-Things” (IoT) has been increasingly prevalent in the forecast of future electronics. From monitoring the environment and machines around us to the human body, IoT envisions electronics physically present in every aspect of our daily lives. While some devices may be realized on rigid silicon, there is a need for electronics with new non-planar form factors^{1,2}, which are thin and light, and can be conformally attached to objects with unusual shapes, on the human skin, or even implanted into the human body¹. With these applications in mind, we need to realize electronics on flexible substrates that are robust to mechanical strain, easy to integrate, and capable of low-power consumption and high performance at the nanoscale^{2,3}.

Recent studies have suggested that 2D materials are good candidates for flexible substrates, because of their lack of dangling bonds, good carrier mobility in atomically thin (sub-1 nm) layers, reduced

short-channel effects, and easy transfer onto arbitrary substrates^{2,4-7}. Among these candidates, monolayer transition metal dichalcogenides (TMDs) like MoS₂ are well-suited for low-power applications due to their good electronic band gaps (~ 2 eV)^{8,9} which enable low off-currents ($\sim \text{fA } \mu\text{m}^{-1}$)^{10,11}. However, the performance of flexible TMD transistors with nanoscale channel lengths is still elusive because of the difficulty of realizing such dimensions on flexible substrates¹², and due to TMD transfer processes which leave contamination or cause damage to the atomically-thin material¹³⁻¹⁵. The shortest flexible MoS₂ transistors (~ 68 nm) reported to date used 3-layer exfoliated material with on-currents of $135 \mu\text{A } \mu\text{m}^{-1}$, ostensibly limited by their contact resistance¹⁶. For large-scale practical applications, MoS₂ must be synthesized by chemical vapor deposition (CVD), and the shortest channel (gate) reported was ~ 750 nm (~ 500 nm) with $85 \mu\text{A } \mu\text{m}^{-1}$ on-current, also contact-limited¹⁷. There have been only a limited number of reports on flexible TMD field-effect transistors (FETs) other than MoS₂, including flexible WSe₂ FETs¹⁸⁻²¹ and, to our knowledge, none on flexible MoSe₂ FETs to date.

In this work, we demonstrate flexible monolayer MoS₂ transistors with on-currents up to $470 \mu\text{A } \mu\text{m}^{-1}$ at $V_{\text{DS}} = 1$ V in sub-100 nm channels, which is the highest reported to date for flexible MoS₂ FETs. These devices are achieved with a new transfer process for TMDs onto flexible substrates, including lithographically predefined metal contacts. The TMD is grown by high-quality CVD on a SiO₂/Si substrate and the critical contact separation is defined while the channel is still on the rigid substrate, enabling the nanoscale devices. Flexible polyimide (PI) is spin-coated onto the pre-patterned structures and all are released together, with the remaining process continuing on the PI. This approach enables record-achieving flexible FETs with MoS₂ and WSe₂, and the first flexible MoSe₂ transistors, all in the staggered configuration²², i.e., with the channel sandwiched between source/drain and gate.

Transfer Process with Embedded Contacts

The TMDs were grown on SiO₂/Si substrates using chemical vapor deposition (CVD) as previously reported²³⁻²⁶. Subsequently, we lithographically patterned Au metal contacts on top. We chose Au because of its good contact resistance²⁷ (R_{C}) to MoS₂ and its low adhesion²⁸ to SiO₂. Hence, both Au and the TMD (lacking out-of-plane dangling bonds) can be released from SiO₂ surfaces without damage, as shown below. After the definition of the metal contacts, we conformally cover the pre-patterned structures with $\sim 5 \mu\text{m}$ thick PI which is released together with the TMD and metal from the SiO₂/Si growth substrate, by immersion and agitation in DI water (additional details are provided in Methods).

Fig. 1a shows the processed SiO₂/Si substrate with TMD, contacts, and PI, Fig. 1b displays the release schematic, and Fig. 1c shows the transparent PI substrate after release. We note that a similar damage-

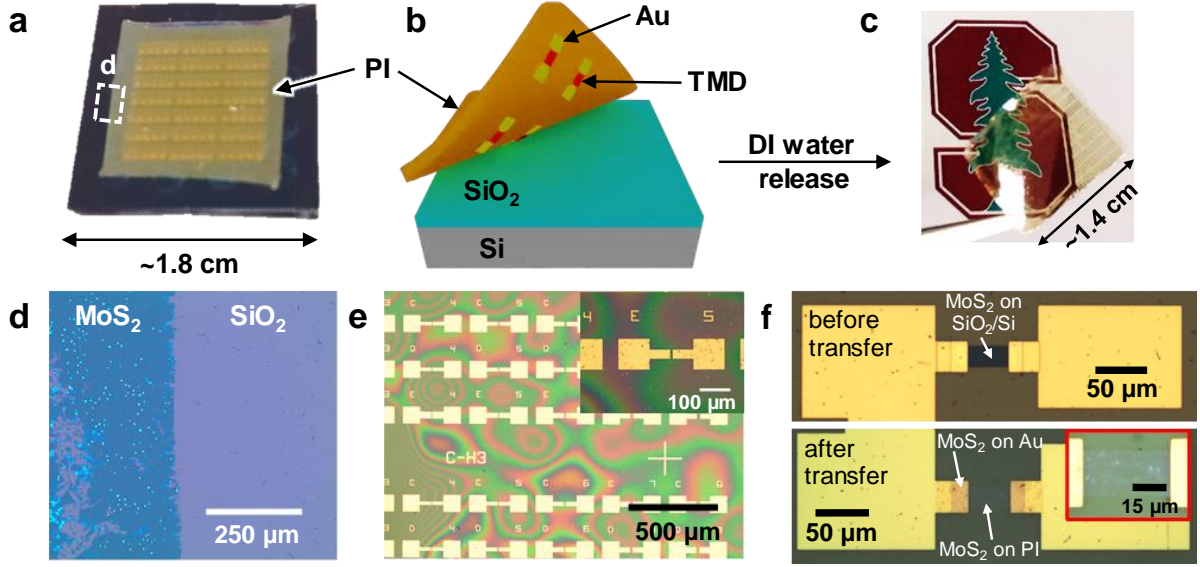


Fig. 1 | Transfer process for 2D monolayers with contacts. **a**, Optical image of MoS₂ and patterned metal covered by polyimide (PI) on SiO₂/Si. **b**, Schematic of the transfer process: the PI with embedded metal contacts and monolayer TMD are released from the rigid growth substrate. **c**, Optical image of the flexible PI after transfer. Optical microscope images of **d**, the SiO₂/Si growth substrate after transfer (with the bare SiO₂ surface where MoS₂ had previously been covered by PI), **e**, PI film with contacts and unpatterned MoS₂ after transfer and **f**, contacts with patterned MoS₂ on SiO₂/Si (top) and PI (bottom). Raman and photoluminescence (PL) spectra of MoS₂, WSe₂, MoSe₂ before and after transfer are shown in Supplementary Section B.

free transfer of MoS₂ layers (without contacts) for coplanar²² micron-sized FETs has recently been demonstrated over 4-inch wafers²⁹, indicating this approach could be scaled up.

The microscope image in Fig. 1d shows that the TMD (here MoS₂) is completely delaminated from the area that had been covered by PI on the SiO₂/Si substrate. We can transfer continuous (Fig. 1e) as well as pre-patterned (Fig. 1f) MoS₂ films with embedded contacts, enabling us to realize devices based on several fabrication approaches. As shown later, we fabricated FETs with MoS₂, MoSe₂ and WSe₂, where only the contacts were patterned before transfer, minimizing process steps on unprotected TMDs (Fig. 1e and Supplementary Fig. S1), but leading to channel widths greater than the electrode widths (referred to as *Type A* devices). We also realized FETs where the MoS₂ channel was predefined by reactive ion etching (RIE) before transfer (Fig. 1f), which enables accurate channel width definition (referred to as *Type B*). Further details on device fabrication can be found in the Methods.

To confirm that the TMDs remain intact throughout the transfer process, we performed extensive Raman spectroscopy and photoluminescence (PL) measurements before and after transfer (Supplementary Fig. S2 and Section B). We observed that PI background signal and quenching on Au surfaces^{30,31}

affect the resolution and visibility of TMD peaks. The Raman and PL spectra on SiO₂/Si indicate TMDs with monolayer thickness, however, MoSe₂ also had regions with bilayers (see Supplementary Section B). Generally, the absence of major changes in Raman and PL before/after transfer indicates that mono- as well as multilayer TMDs can be readily transferred with this technique, without apparent damage. The electrical results presented below further confirm the excellent viability of this transfer approach.

Flexible Top-Gated Field-Effect Transistors

After the transfer process, the source/drain contacts are now embedded in the PI substrate and the TMD semiconductor is on top. To prevent contamination of this exposed TMD surface, we deposit an Al₂O₃ gate dielectric immediately after the transfer process and prior to any other patterning steps. The fabrication process is finalized with the gate metal definition, leading to a staggered device geometry. For MoS₂ FETs of *Type A*, we employ RIE to pattern the channel and gate dielectric together after the gate metal deposition, and additional fabrication details are given in Methods. The device cross-section is schematically shown in Fig. 2a and Fig. 2b-d display optical images of the WSe₂, MoSe₂ and MoS₂ FETs. Measured transfer and output characteristics of micron-scale FETs with WSe₂, MoSe₂ (both *Type A*) and MoS₂ (*Type B*) are presented in Fig. 2e-j, respectively, all displaying *n*-type behavior.

The extracted device parameters for all TMDs are listed in Table 1. Threshold voltage V_T and extrinsic field-effect mobility $\mu_{FE,ext}$ were estimated at the maximum transconductance (g_m), using the measured Al₂O₃ gate oxide capacitance ($C_{ox} = 0.21$ to $0.32 \mu F cm^{-2}$) from the TMD FETs obtained in accumulation (see Supplementary Fig. S7)³². The 2 μm long monolayer WSe₂ FET exhibits a maximum on-current $I_D = 3.5 \pm 0.05 \mu A \mu m^{-1}$ (the source of the error bars is explained below) at a drain-source voltage $V_{DS} = 1 V$, which is over twice larger than the highest previously reported for flexible WSe₂ (using bilayer exfoliated material)¹⁸. The 3 μm long MoSe₂ FET reaches $I_D = 4.2 \pm 0.34 \mu A \mu m^{-1}$ at $V_{DS} = 4 V$, which is to our knowledge the first demonstration of flexible MoSe₂ FETs.

The mobility and width-normalized current of *Type A* devices are listed with error bars because in these the channel width was not patterned and they were subject to (some) current spreading effects, which we account for with numerical simulations (see Supplementary Section K). For example, the unpatterned hexagonal crystals for the selenide-based FETs can be seen in Fig. 2b,c. Their measured data are shown in plain current units (μA) in Fig. 2e,f and Fig. 2h,i, respectively, but the error bars are included when presenting their width-normalized current ($\mu A/\mu m$), e.g. in Table 1.

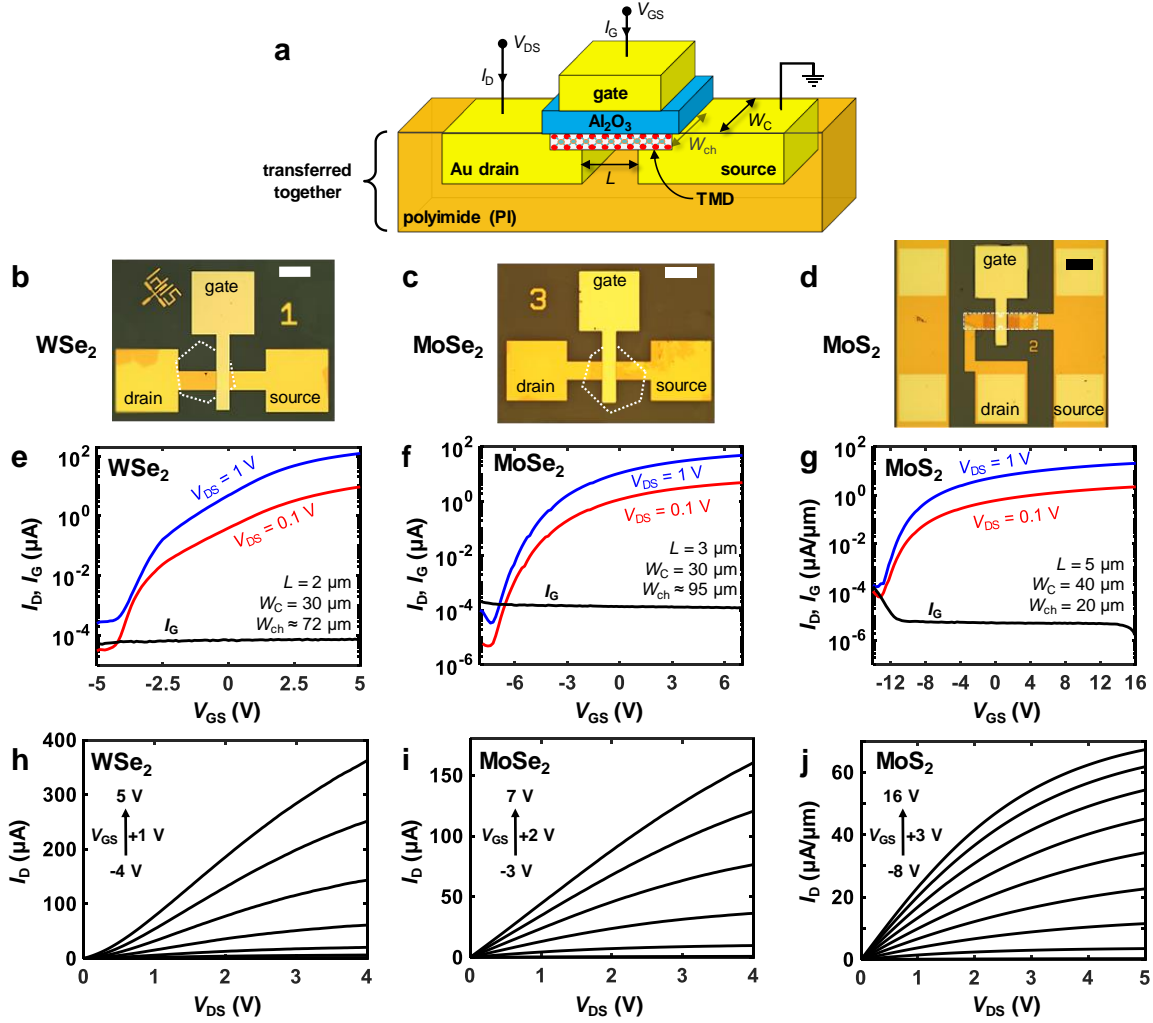


Fig. 2 | Flexible field-effect transistors (FETs) with transition metal dichalcogenides (TMDs). **a**, Schematic cross-section. Optical microscope images of FETs with **b**, WSe₂ (Type A), **c**, MoSe₂ (Type A) and **d**, MoS₂ (Type B), scale bars: 50 μm . Measured transfer and output characteristics of **e**, **h**, WSe₂ (Type A), **f**, **i**, MoSe₂ (Type A) and **g**, **j**, MoS₂ (Type B). The gate current (I_{g}) is often negligible, although for some devices it can limit the on/off ratio.

The correction is not needed for our *Type B* devices because of the optimized geometry and modified fabrication process. Hence, Fig. 2g,j for *Type B* MoS₂ FETs are displayed in width-normalized units and the better quality of this material also enables larger $I_{\text{D}} \approx 67.3 \text{ } \mu\text{A } \mu\text{m}^{-1}$ in a 5 μm long FET at $V_{\text{DS}} = 5 \text{ V}$. In comparison, *Type A* MoS₂ FETs had higher subthreshold swing SS and off-current, reducing their on/off ratio (Table 1 and Supplementary Fig. S8). Comparing device hysteresis³³, we find it ranges from $\sim 0.1 \text{ V}$ (WSe₂) to $\sim 1.6 \text{ V}$ (MoSe₂) for all devices and TMDs, indicating that the additional patterning step of *Type B* devices does not deteriorate TMD interfaces (see Supplementary Fig. S9). We have also verified the stability of the flexible TMD FETs under tensile bending and found negligible changes for a bending radius of 4 mm (Supplementary Fig. S10).

Device	Channel Length (nm)	$\mu_{\text{FE,ext}}$ ($\text{cm}^2\text{V}^{-1}\text{s}^{-1}$)	I_{D} at $V_{\text{DS}} = 1\text{V}$ ($\mu\text{A } \mu\text{m}^{-1}$)	V_{T} (V)	SS (mV decade^{-1})	on/off ratio
WSe ₂ (Type A)	2000	$4.9 \pm 0.07^*$	$3.5 \pm 0.05^*$	1.6	380	3×10^5
MoSe ₂ (Type A)	3000	$1.4 \pm 0.09^*$	$1.3 \pm 0.09^*$	-2	430	10^6
MoS ₂ (Type A)	5000	$15 \pm 2.2^*$	$5.4 \pm 0.79^*$	3.9	1700	3.6×10^3
MoS ₂ (Type B)	5000	25.7	21	-5.2	850	10^5
MoS ₂ (Type B)	100	7.2	229	0.6	730	2×10^6
MoS ₂ (Type A)	70	$20 \pm 1.4^*$	$470 \pm 45^*$	6	1000	4×10^3

Table 1 | Electrical parameters of flexible FETs. The extrinsic field-effect mobility $\mu_{\text{FE,ext}}$ and threshold voltage V_{T} , were extracted from the maximum g_{m} in the linear FET operating regime at a drain-source voltage $V_{\text{DS}} = 100$ mV. The subthreshold swing (SS) value denotes the extracted minimum. We note some V_{T} variability, which is not unusual for 2D channels in academic fabrication facilities (also see Supplementary Fig. S15). * indicates values corrected for current spreading.

Nanoscale MoS₂ Flexible Transistors

As MoS₂ has the most mature growth process with the highest electrical quality and best surface coverage, we further studied its FET scaling down to ~ 50 nm with electron-beam lithography (EBL) for source/drain contact patterning. Importantly, this nanoscale resolution is enabled by our approach wherein the contact patterning is first performed on the atomically smooth SiO₂/Si surface instead of the PI, which is prone to waviness, enhanced charging effects, and possible damage in EBL³⁴. We also verified that this process is benign to MoS₂, performing Raman and PL measurements before and after EBL, finding no apparent evidence of damage to MoS₂ (Supplementary Section G). The remaining device fabrication and transfer were performed as described above.

Fig. 3a displays a top view optical image of a nanoscale channel after transfer, and a post-fabrication device cross-section. The cross-section reveals the Al₂O₃ gate dielectric covers the planar source/drain electrodes, including the ~ 100 nm nanogap between them, illustrating the absence of “steps” in surface topography enabled by this fabrication technique with contacts embedded in the flexible substrate. Electrical measurements of a similar *Type B* device with 100 nm long channel are shown in Fig. 3b,c revealing good on/off ratio ($> 10^6$), high $I_{\text{D}} \approx 303 \mu\text{A } \mu\text{m}^{-1}$ (at $V_{\text{DS}} = 1.4$ V) and $\mu_{\text{FE,ext}} \approx 7.2 \text{ cm}^2\text{V}^{-1}\text{s}^{-1}$. The mobility appears smaller than in micron-scale devices due to greater contribution from contact resistance, as discussed below (for other device parameters see Table 1). Measured output characteristics (Fig. 3c) show signs of self-heating and velocity saturation^{7,35} due to the onset of current saturation

at lower V_{DS} with higher gate-source voltages V_{GS} , which is similar to the self-heating of MoS₂ FETs on SiO₂/Si substrates. We estimate the temperature of this FET reaches $\sim 172^\circ\text{C}$ at the peak input power shown in Fig. 3c (see Supplementary Section H), and the Au contacts are primarily responsible for lateral heat spreading from the nanoscale device channel.

To gain additional insight into intrinsic device parameters, we extracted I_D (at an overdrive $V_{ov} = V_{GS} - V_T = 8\text{ V}$) and $\mu_{FE,ext}$ for channel lengths from 50 nm to 10 μm in Fig. 3d,e. Measuring numerous devices allows us to comment both on “typical” and “best case” device performance. We use a model which relates I_D and $\mu_{FE,ext}$ to L , R_C , and the intrinsic field-effect mobility μ_{FE} . (The adapted model³⁶,

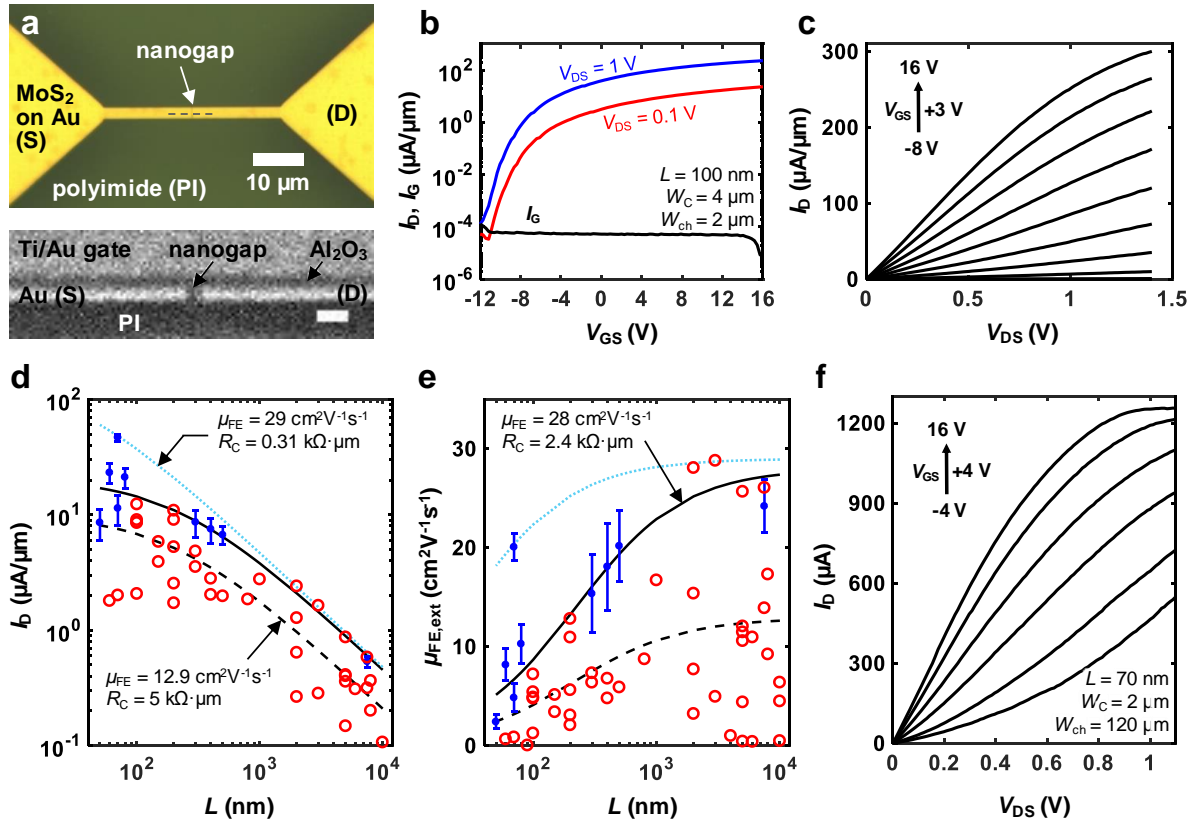


Fig. 3 | Nanoscale MoS₂ field-effect transistors (FETs). **a**, Optical microscope image of a nanoscale channel after transfer (top) and cross-section scanning electron microscope (SEM) image of a transistor with a channel length (L) = 100 nm (bottom, scale bar: 200 nm). The cross-section is taken at the dashed line in the top image. **b**, Transfer and **c**, output characteristics of a *Type B* MoS₂ FET with $L = 100\text{ nm}$. **d**, Drain current I_D and **e**, extrinsic field-effect mobility $\mu_{FE,ext}$ as a function of L for ~ 50 devices at a drain-source voltage $V_{DS} = 0.1\text{ V}$. I_D is displayed at an overdrive voltage $V_{GS} - V_T = 8\text{ V}$ and $\mu_{FE,ext}$ was extracted at the maximum transconductance. Solid black and dashed black lines illustrate a fitted trend for “best” and “typical” *Type B* devices (red circles), while the blue dotted line combines best results for all FETs, including *Type A* devices (blue). **f**, Electrical characteristics of a MoS₂ FET (*Type A*) with $L = 70\text{ nm}$ showing remarkably high $I_D > 1.2\text{ mA}$, which is $\sim 470\text{ }\mu\text{A }\mu\text{m}^{-1}$ after current spreading correction.

the V_T and $\mu_{FE,ext}$ extractions are described in Supplementary Sections C and J.) Fig. 3d,e reveals that I_D plateaus and $\mu_{FE,ext}$ decreases at sub-1 μm channel lengths, which clearly indicates these devices are limited by R_C . The dashed black lines show the model for “typical” *Type B* devices (red circles) which we fitted with an average μ_{FE} ($\sim 12.9 \text{ cm}^2 \text{V}^{-1} \text{s}^{-1}$) for micron-scale devices where the impact of R_C is small, and by setting $R_C = 5 \text{ k}\Omega \mu m$ to follow the middle of the distribution for shorter L .

The solid black lines in Fig. 3d,e are based on a similar approach but using higher μ_{FE} ($\sim 28 \text{ cm}^2 \text{V}^{-1} \text{s}^{-1}$) to fit the best-performing *Type B* devices with $R_C = 2.4 \text{ k}\Omega \mu m$. Taking into account also “best” *Type A* devices (blue symbols and error bars, corrected for current spreading), we fit $R_C \approx 310 \Omega \mu m$ for one device (at $L = 70 \text{ nm}$) and a slightly higher $\mu_{FE} = 29 \text{ cm}^2 \text{V}^{-1} \text{s}^{-1}$, generating the blue dotted lines. The FET with highest on-current achieves an impressive $I_D = 470 \pm 45 \mu A \mu m^{-1}$ at $V_{DS} = 1 \text{ V}$ (see Supplementary Section I for electrical data and Supplementary Section K for current spreading correction), and its electrical characteristics are shown in Fig. 3f and Supplementary Fig. S14b. The presence of a “hero” device is not surprising when one hundred (or two hundred²⁴) devices are measured, being both an indicator of academic fabrication variability, and of the promise of these 2D semiconductors if variability challenges are mitigated by industrial optimization. (We note that our *Type A* and *Type B* devices have similar variability, also see Supplementary Section I.)

Our estimated best-case μ_{FE} and R_C are comparable to best reported values for monolayer MoS_2 on flexible substrates and on SiO_2/Si rigid substrates, respectively^{17,24,35}. The highest on-current I_D is over three times greater than in previous reports for flexible MoS_2 FETs¹⁶, similar to the best TMD FETs on rigid substrates³⁷, and even comparable to flexible FETs based on graphene³⁸ and c-Si³⁹. Moreover, this fabrication technique enables us to scale flexible MoS_2 FETs to the shortest channel lengths reported to date (Supplementary Fig. S14c).

Fig. 4 displays benchmarking of our flexible MoS_2 transistors compared to other technologies on flexible substrates. Displaying $\mu_{FE,ext}$ and I_D (at $V_{DS} = 1 \text{ V}$, unless noted otherwise) for flexible MoS_2 FETs vs. L (Fig. 4a,b) reveals that nanoscale devices have received little attention until now (values listed in Supplementary Table S1)^{4,16,17,29,40-49}. Fig. 4c compares the on-current and on/off ratio of the few existing sub-200 nm flexible FETs (at $V_{DS} = 0.5 \text{ V}$, unless noted otherwise) revealing good performance of our MoS_2 even next to high-mobility materials (values listed in Supplementary Table S2)^{39,50-54}. The on/off ratio of MoS_2 is many orders of magnitude higher than graphene, making MoS_2 FETs much more suitable for low-power applications among 2D channel materials. Compared to flexible c-Si FETs, flexible TMD FETs have a fundamentally different structure, with a sub-nanometer thin channel

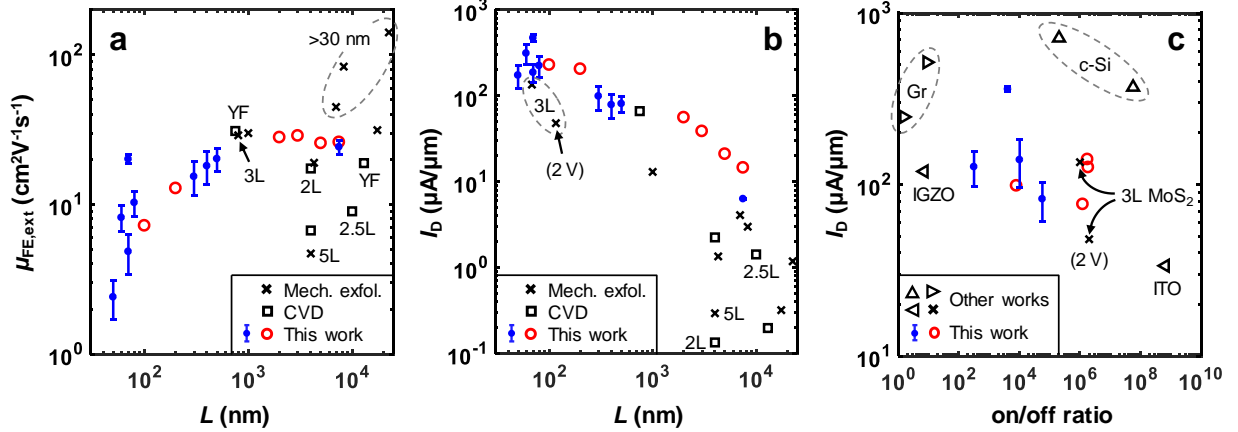


Fig. 4 | Benchmarking flexible FETs. **a**, Extrinsic field-effect mobility $\mu_{FE,ext}$ and **b**, drain current I_D (at $V_{DS} = 1$ V) for flexible MoS₂ transistors as a function of channel length (L)^{4,16,17,29,40-49}. Three studies reported μ_{FE} excluding contact resistance with the y-function method (“YF”). A few points correspond to 3-layer (3L) MoS₂, one of them at $V_{DS} = 2$ V, one ($L = 68$ nm) at unspecified voltage. Most CVD-grown MoS₂ are monolayers (1L), including this work, the other thicknesses are as labeled up to 5-layers (5L), and unlabeled points are all thicker exfoliated channels. All thicknesses and more details are listed in Supplementary Section L. **c**, Reported I_D (at $V_{DS} = 0.5$ V) vs. on/off ratio for flexible FETs^{39,50-54} with channel $L \leq 200$ nm. For comparison, two data points are shown for graphene (“Gr”), two for crystalline silicon (“c-Si”), two for oxide semiconductors (ITO and IGZO), and the others are for MoS₂ (our CVD monolayer data and two reports on 3L exfoliated).

without out-of-plane dangling bonds. This enables shorter channel lengths, better mechanical robustness, and potentially lower cost (due to simple transfer processes), all advantageous for higher-performance and lower-power operation on flexible substrates.

Conclusion

In summary, we demonstrated high-performance MoS₂ transistors on flexible substrates, with a novel transfer process which enabled making the shortest channels to date (~50 nm). We reached drive currents up to 470 $\mu\text{A } \mu\text{m}^{-1}$ ($L = 70$ nm, at $V_{DS} = 1$ V), among the highest for any monolayer 2D semiconductor, including those on rigid SiO₂/Si substrates, and comparable to those of flexible graphene and c-Si transistors. The high current is achieved despite the low thermal conductivity of the PI substrate, as the short channel devices benefit from heat spreading by the Au contacts. We also applied the fabrication technique to other 2D semiconductors, reporting the first flexible MoSe₂ FETs and the highest current in flexible WSe₂ FETs. This fabrication approach could become a template for making flexible transistors with other materials where few short-channel demonstrations exist (e.g., oxides, organics, or carbon nanotubes). Together with further optimization of electrostatic control (thinner gate dielectrics or double-gates) and reduced parasitics (e.g., lower R_C) these results provide a promising outlook for incorporating flexible TMD electronics in low-power and high-performance IoT applications.

References

1. He, J., Nuzzo, R. G. & Rogers, J. A. Inorganic materials and assembly techniques for flexible and stretchable electronics. *Proc. IEEE* **103**, 619-632 (2015).
2. Akinwande, D., Petrone, N. & Hone, J. Two-dimensional flexible nanoelectronics. *Nat. Commun.* **5**, 5678 (2014).
3. Myny, K. The development of flexible integrated circuits based on thin-film transistors. *Nat. Electron.* **1**, 30-39 (2018).
4. Salvatore, G. A. *et al.* Fabrication and transfer of flexible few-layers MoS₂ thin film transistors to any arbitrary substrate. *ACS Nano* **7**, 8809-8815 (2013).
5. Gurarslan, A. *et al.* Surface-energy-assisted perfect transfer of centimeter-scale monolayer and few-layer MoS₂ films onto arbitrary substrates. *ACS Nano* **8**, 11522-11528 (2014).
6. Nourbakhsh, A. *et al.* MoS₂ field-effect transistor with sub-10 nm channel length. *Nano Lett.* **16**, 7798-7806 (2016).
7. Liu, H., Neal, A. T. & Ye, P. D. Channel length scaling of MoS₂ MOSFETs. *ACS Nano* **6**, 8563-8569 (2012).
8. Gusakova, J. *et al.* Electronic properties of bulk and monolayer TMDs: theoretical study within DFT framework (GVJ-2e method). *Phys. Status Solidi (a)* **214**, 1700218 (2017).
9. Ryou, J., Kim, Y.-S., Santosh, K. & Cho, K. Monolayer MoS₂ bandgap modulation by dielectric environments and tunable bandgap transistors. *Sci. Rep.* **6**, 29184 (2016).
10. Kshirsagar, C. U. *et al.* Dynamic memory cells using MoS₂ field-effect transistors demonstrating femtoampere leakage currents. *ACS Nano* **10**, 8457-8464 (2016).
11. Illarionov, Y. Y. *et al.* Annealing and encapsulation of CVD-MoS₂ FETs with 10¹⁰ on/off current ratio. In *2018 76th Device Research Conference (DRC)* 1-2 (IEEE, 2018), DOI: 10.1109/DRC.2018.8442242.
12. Münzenrieder, N., Cantarella, G. & Petti, L. Fabrication and AC performance of flexible indium-gallium-zinc-oxide thin-film transistors. *ECS Trans.* **90**, 55-63 (2019).
13. Pu, J. *et al.* Highly flexible MoS₂ thin-film transistors with ion gel dielectrics. *Nano Lett.* **12**, 4013-4017 (2012).
14. Ma, D. *et al.* A universal etching-free transfer of MoS₂ films for applications in photodetectors. *Nano Res.* **8**, 3662-3672 (2015).
15. Zhang, T. *et al.* Clean transfer of 2D transition metal dichalcogenides using cellulose acetate for atomic resolution characterizations. *ACS Appl. Nano Mater.* **2**, 5320-5328 (2019).
16. Cheng, R. *et al.* Few-layer molybdenum disulfide transistors and circuits for high-speed flexible electronics. *Nat. Commun.* **5**, 5143 (2014).
17. Chang, H. Y. *et al.* Large-area monolayer MoS₂ for flexible low-power RF nanoelectronics in the GHz regime. *Adv. Mater.* **28**, 1818-1823 (2016).
18. Das, S., Gulotty, R., Sumant, A. V. & Roelofs, A. All two-dimensional, flexible, transparent, and thinnest thin film transistor. *Nano Lett.* **14**, 2861-2866 (2014).
19. Podzorov, V., Gershenson, M., Kloc, C., Zeis, R. & Bucher, E. High-mobility field-effect transistors based on transition metal dichalcogenides. *Appl. Phys. Lett.* **84**, 3301-3303 (2004).
20. Qiu, H. *et al.* Simultaneous optical tuning of hole and electron transport in ambipolar WSe₂ interfaced with a bicomponent photochromic layer: from high-mobility transistors to flexible multilevel memories. *Adv. Mater.* **32**, 1907903 (2020).
21. Pu, J. *et al.* Highly flexible and high-performance complementary inverters of large-area transition metal dichalcogenide monolayers. *Adv. Mater.* **28**, 4111-4119 (2016).
22. Fortunato, E., Barquinha, P. & Martins, R. Oxide semiconductor thin-film transistors: a review of recent advances. *Adv. Mater.* **24**, 2945-2986 (2012).
23. Smithe, K. K., English, C. D., Suryavanshi, S. V. & Pop, E. Intrinsic electrical transport and performance projections of synthetic monolayer MoS₂ devices. *2D Mater.* **4**, 011009 (2017).

24. Smithe, K. K., Suryavanshi, S. V., Muñoz Rojo, M., Tedjarati, A. D. & Pop, E. Low variability in synthetic monolayer MoS₂ devices. *ACS Nano* **11**, 8456-8463 (2017).
25. Smithe, K. K. *et al.* Nanoscale heterogeneities in monolayer MoSe₂ revealed by correlated scanning probe microscopy and tip-enhanced Raman spectroscopy. *ACS Appl. Nano Mater.* **1**, 572-579 (2018).
26. Chen, J. *et al.* Plasmon-resonant enhancement of photocatalysis on monolayer WSe₂. *ACS Photonics* **6**, 787-792 (2019).
27. English, C. D., Shine, G., Dorgan, V. E., Saraswat, K. C. & Pop, E. Improved contacts to MoS₂ transistors by ultra-high vacuum metal deposition. *Nano Lett.* **16**, 3824-3830 (2016).
28. George, M., Bao, Q., Sorensen, I., Glaunsinger, W. & Thundat, T. Thermally induced changes in the resistance, microstructure, and adhesion of thin gold films on Si/SiO₂ substrates. *J. Vac. Sci. Technol. A* **8**, 1491-1497 (1990).
29. Shinde, S. M. *et al.* Surface-functionalization-mediated direct transfer of molybdenum disulfide for large-area flexible devices. *Adv. Funct. Mater.* **28**, 1706231 (2018).
30. Daus, A. *et al.* Metal-halide perovskites for gate dielectrics in field-effect transistors and photodetectors enabled by PMMA lift-off process. *Adv. Mater.* **30**, 1707412 (2018).
31. Bhanu, U., Islam, M. R., Tetard, L. & Khondaker, S. I. Photoluminescence quenching in gold-MoS₂ hybrid nanoflakes. *Sci. Rep.* **4**, 5575 (2014).
32. Knobelspies, S. *et al.* Geometry-based tunability enhancement of flexible thin-film varactors. *IEEE Electron Device Lett.* **38**, 1117-1120 (2017).
33. Datye, I. M. *et al.* Reduction of hysteresis in MoS₂ transistors using pulsed voltage measurements. *2D Mater.* **6**, 011004 (2019).
34. Scholten, K. & Meng, E. Electron-beam lithography for polymer bioMEMS with submicron features. *Microsyst. & Nanoeng.* **2**, 16053 (2016).
35. Smithe, K. K., English, C. D., Suryavanshi, S. V. & Pop, E. High-field transport and velocity saturation in synthetic monolayer MoS₂. *Nano Lett.* **18**, 4516-4522 (2018).
36. Münzenrieder, N. *et al.* Contact resistance and overlapping capacitance in flexible sub-micron long oxide thin-film transistors for above 100 MHz operation. *Appl. Phys. Lett.* **105**, 263504 (2014).
37. McClellan, C. J., Suryavanshi, S. V., English, C. D., Smithe, K.K.H., Bailey, C. S., Grady, R. W. & Pop, E. *2D Device Trends*. <http://2d.stanford.edu/2D_Trends.html>, (accessed on July 14, 2020), [Online].
38. Lan, Y. *et al.* Flexible graphene field-effect transistors with extrinsic f_{\max} of 28 GHz. *IEEE Electron Device Lett.* **39**, 1944-1947 (2018).
39. Shahrjerdi, D. *et al.* Advanced flexible CMOS integrated circuits on plastic enabled by controlled spalling technology. In *2012 Int. Electron Devices Meeting (IEDM)* 5.1. 1-5.1. 4 (IEEE, 2012), DOI: 10.1109/IEDM.2012.6478981.
40. Kwon, H. *et al.* Selective and localized laser annealing effect for high-performance flexible multilayer MoS₂ thin-film transistors. *Nano Res.* **7**, 1137-1145 (2014).
41. Chang, H.-Y. *et al.* High-performance, highly bendable MoS₂ transistors with high-k dielectrics for flexible low-power systems. *ACS Nano* **7**, 5446-5452 (2013).
42. Yoon, J. *et al.* Highly flexible and transparent multilayer MoS₂ transistors with graphene electrodes. *Small* **9**, 3295-3300 (2013).
43. Lee, G.-H. *et al.* Flexible and transparent MoS₂ field-effect transistors on hexagonal boron nitride-graphene heterostructures. *ACS Nano* **7**, 7931-7936 (2013).
44. Yoo, G. *et al.* Real-time electrical detection of epidermal skin MoS₂ biosensor for point-of-care diagnostics. *Nano Res.* **10**, 767-775 (2017).
45. Song, W. G. *et al.* High-performance flexible multilayer MoS₂ transistors on solution-based polyimide substrates. *Adv. Funct. Mater.* **26**, 2426-2434 (2016).
46. Ma, J., Choi, K.-Y., Kim, S. H., Lee, H. & Yoo, G. All polymer encapsulated, highly-sensitive MoS₂ phototransistors on flexible PAR substrate. *Appl. Phys. Lett.* **113**, 013102 (2018).
47. Amani, M., Burke, R. A., Proie, R. M. & Dubey, M. Flexible integrated circuits and multifunctional electronics based on single atomic layers of MoS₂ and graphene. *Nanotechnology* **26**, 115202 (2015).

48. Woo, Y. *et al.* Large-area CVD-grown MoS₂ driver circuit array for flexible organic light-emitting diode display. *Adv. Electron. Mater.* **4**, 1800251 (2018).
49. Park, Y. J. *et al.* All MoS₂-based large area, skin-attachable active-matrix tactile sensor. *ACS Nano* **13**, 3023-3030 (2019).
50. Zhai, Y., Mathew, L., Rao, R., Xu, D. & Banerjee, S. K. High-performance flexible thin-film transistors exfoliated from bulk wafer. *Nano Lett.* **12**, 5609-5615 (2012).
51. Park, S. *et al.* Extremely high-frequency flexible graphene thin-film transistors. *IEEE Electron Device Lett.* **37**, 512-515 (2016).
52. Yeh, C.-H. *et al.* Gigahertz flexible graphene transistors for microwave integrated circuits. *ACS Nano* **8**, 7663-7670 (2014).
53. Wang, M. *et al.* High performance gigahertz flexible radio frequency transistors with extreme bending conditions. In *2019 IEEE Int. Electron Devices Meeting (IEDM)* 8.2. 1-8.2. 4 (IEEE, 2019), DOI: 10.1109/IEDM19573.2019.8993531.
54. Münzenrieder, N. *et al.* Focused ion beam milling for the fabrication of 160 nm channel length IGZO TFTs on flexible polymer substrates. *Flex. Print. Electron.* **5**, 015007 (2020).

Methods

Raman and Photoluminescence measurements

The Raman and PL measurements were performed on a HORIBA Scientific LabRAM HR Evolution spectrometer using an excitation wavelength of 532 nm. For Raman measurements on SiO₂/Si, an acquisition time, accumulations, laser power and optical grating of 5 s, 3, 0.14 mW, 1800 gr/mm were used, and the spot size is less than 1 μ m. For the Raman measurements after transfer on PI or Au/PI surfaces, the acquisition time was increased to 45 s, while the other parameters remained the same. For PL measurements on SiO₂/Si, PI and Au/PI, an acquisition time, accumulations, laser power and optical grating of 5 s, 3, 0.14 mW, 600 gr/mm were used.

Device fabrication including transfer process

Fabrication of device Type A: The TMDs were grown on Si/SiO₂ substrates involving solid-source chemical vapor deposition (CVD) as previously reported²³⁻²⁶. The device fabrication was performed in the Stanford Nanofabrication Facility and Stanford Nano Shared Facilities. First, a 45 nm thick Au source/drain contact metal was deposited and patterned by electron-beam evaporation and lift-off. Optionally, the adhesion of the metal contacts to the later spin-coated PI layer can be improved by evaporating an additional Ti layer on top of Au prior to the lift-off, but it is not required. The lithographic patterning for that step was done via optical lithography (Heidelberg MLA 150 direct write lithography tool) for micron scale channel length, and via EBL for sub-micron scale channel lengths. The EBL parameters can be found below. Then, ~5 μ m thick PI layer (PI-2610, HD Microsystems) was spin-coated on top, baked at 90°C and 150°C on a hotplate for each 90 s, and finally cured in a nitrogen

oven at 250°C for 30 minutes. Prior to PI spin-coating, the outside edges of the silicon substrate were protected with tape to facilitate the release of PI from the Si substrate (Fig. 1a). The transfer was performed in DI water by initially mechanically releasing the outside edges with a tweezer followed by agitation until the PI substrate together with the metal contacts and TMD was floating on the DI water surface. After nitrogen blow-drying the substrate, 1.5 nm thick Al blanket film was deposited on top by electron-beam evaporation. This film acts as a seed layer for the subsequent atomic-layer deposition (ALD) of an Al₂O₃ gate dielectric at 200°C. Note, we used 35 nm Al₂O₃ for the MoS₂ devices and 23 nm thick Al₂O₃ for MoSe₂ and WSe₂ devices. This yields $C_{ox} \approx 0.21$ to $0.32 \mu\text{F cm}^{-2}$, directly measured in Supplementary Fig. S7. The oxide thicknesses were chosen to ensure higher device yield and to have numerous FETs for measurement. After the ALD, the gate metal was deposited by electron-beam evaporation of Ti/Au (5/60 nm) and patterned by optical lithography and lift-off. This concluded the fabrication for MoSe₂ and WSe₂ devices. For MoS₂ devices, as a final step the Al₂O₃ and MoS₂ were patterned together using reactive ion etching (Oxford 80 RIE) in CF₄:O₂ at gas flows of 50 sccm:5 sccm, 150 W power and a pressure of 30 mTorr.

Fabrication of device *Type B*: Until the source/drain contact metallization, the fabrication of *Type B* devices was the same as for type A. However, after source/drain metallization the MoS₂ channels were patterned by reactive ion etching (Oxford 80 RIE) in CF₄:O₂ at gas flows of 50 sccm:10 sccm, 100 W power and 30 mTorr pressure, followed by in situ surface cleaning with O₂ plasma (20 W, 10 mTorr, 40 sccm). Then, contact pads and leads were defined by optical lithography, e-beam evaporation of Au/Ti (60 nm/5 nm) and lift-off. This was followed by PI spin-coating, curing and transfer of all structures in the same way as described for device *Type A*. After the gate dielectric deposition (same as for *Type A* devices), via holes for probing source/drain electrodes were wet etched in Al etchant at 40°C. Finally, the gate metallization was done similarly as for device *Type A*.

Electron-beam lithography (EBL) on MoS₂

We used a double layer of poly(methyl methacrylate) (PMMA) for lift-off patterns defined by EBL. The bottom and top layer were 50 nm thick 495K A2 PMMA and 200 nm 950K A4 PMMA, respectively. EBL was performed on a JEOL JBX 6300 lithography system at a dose of $900 \mu\text{C cm}^{-2}$ and an acceleration voltage of 100 kV.

Electrical measurements

All transistors were tested with a Keithley 4200 on a probe station in ambient air. For the bending experiments, the substrates were attached to a metallic cylindrical rod with a radius of 4 mm.

Acknowledgement

A.D. is in part supported by the Swiss National Science Foundation's Early Postdoc.Mobility fellowship (grant P2EZP2_181619) and in part by Beijing Institute of Collaborative Innovation (BICI). R.W.G., C.S.B. and K.S. acknowledge the National Science Foundation (NSF) Graduate Research Fellowship. K.S. also acknowledges the support of the Stanford Graduate Fellowship. All authors thank the Stanford Nanofabrication Facility and Stanford Nano Shared Facilities for enabling device fabrication and characterization, funded under NSF award ECCS-1542152. E.P. and S.V. acknowledge support from the Stanford SystemX Alliance.

Author Contributions

A.D. conceived the work and performed the device fabrication and characterization. A.D. and S.V. developed the TMD transfer process. R.W.G. did the MoS₂ CVD growth and C.S.B. did the WSe₂ and MoSe₂ CVD growths. V.C. carried out the electron beam lithography. A.D. performed optical material analysis with help from K.S and K.B. H.R.L. did the FIB-SEM cross-sections. C.K. set up numerical current spreading simulations and thermal simulations with E.P. A.D. analyzed all data and wrote the manuscript with help from V.C., C.K, and E.P. All authors revised and commented on the manuscript. E.P. supervised the work.

Competing Interests

The authors declare no competing interests.

Supplementary Information

High-Performance Flexible Nanoscale Field-Effect Transistors Based on Transition Metal Dichalcogenides

Alwin Daus¹, Sam Vaziri¹, Victoria Chen¹, Cagil Koroglu¹, Ryan W. Grady¹, Connor S. Bailey¹, Hye Ryoung Lee², Kevin Brenner¹, Kirstin Schauble¹ and Eric Pop^{1,3,*}

¹Department of Electrical Engineering, Stanford University, Stanford, CA 94305, U.S.A.

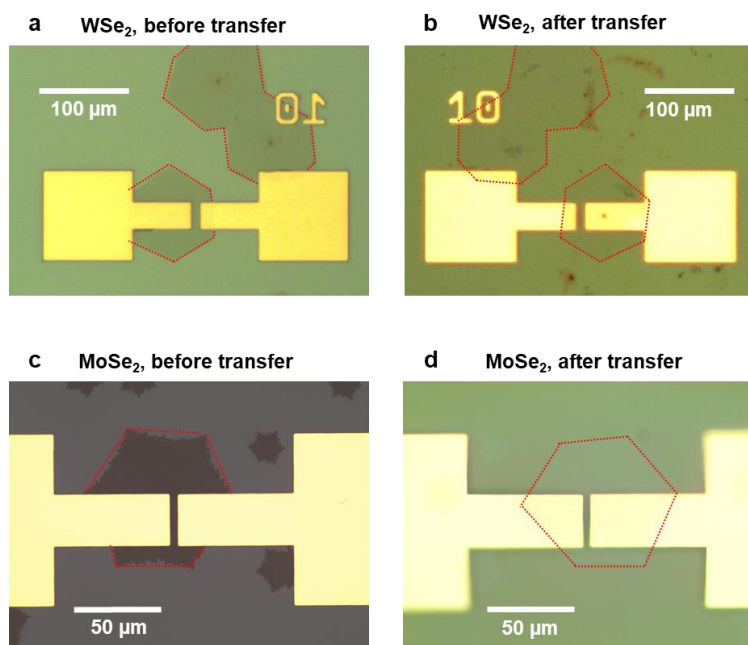
²Geballe Laboratory for Advanced Materials, Stanford University, Stanford, CA 94305, U.S.A.

³Department of Materials Science & Engineering, Stanford University, Stanford, CA 94305, U.S.A.

*Corresponding author email: epop@stanford.edu

A. Optical microscope images for WSe₂ and MoSe₂ before and after the transfer process

Supplementary Fig. S1a,c displays the hexagonally shaped WSe₂ and MoSe₂ crystal grains grown on SiO₂/Si substrates after the patterning of source/drain metal contacts, and *before* the transfer. As visible here, the Au contacts are on top of the TMDs. When the polyimide (PI) is applied on top, it uniformly



Supplementary Fig. S1 | Microscope images of WSe₂ and MoSe₂ with patterned Au metal electrodes. a, WSe₂ on SiO₂/Si before transfer. b, WSe₂ on polyimide (PI) after transfer. c, MoSe₂ on SiO₂/Si before transfer. d, MoSe₂ on PI after transfer.

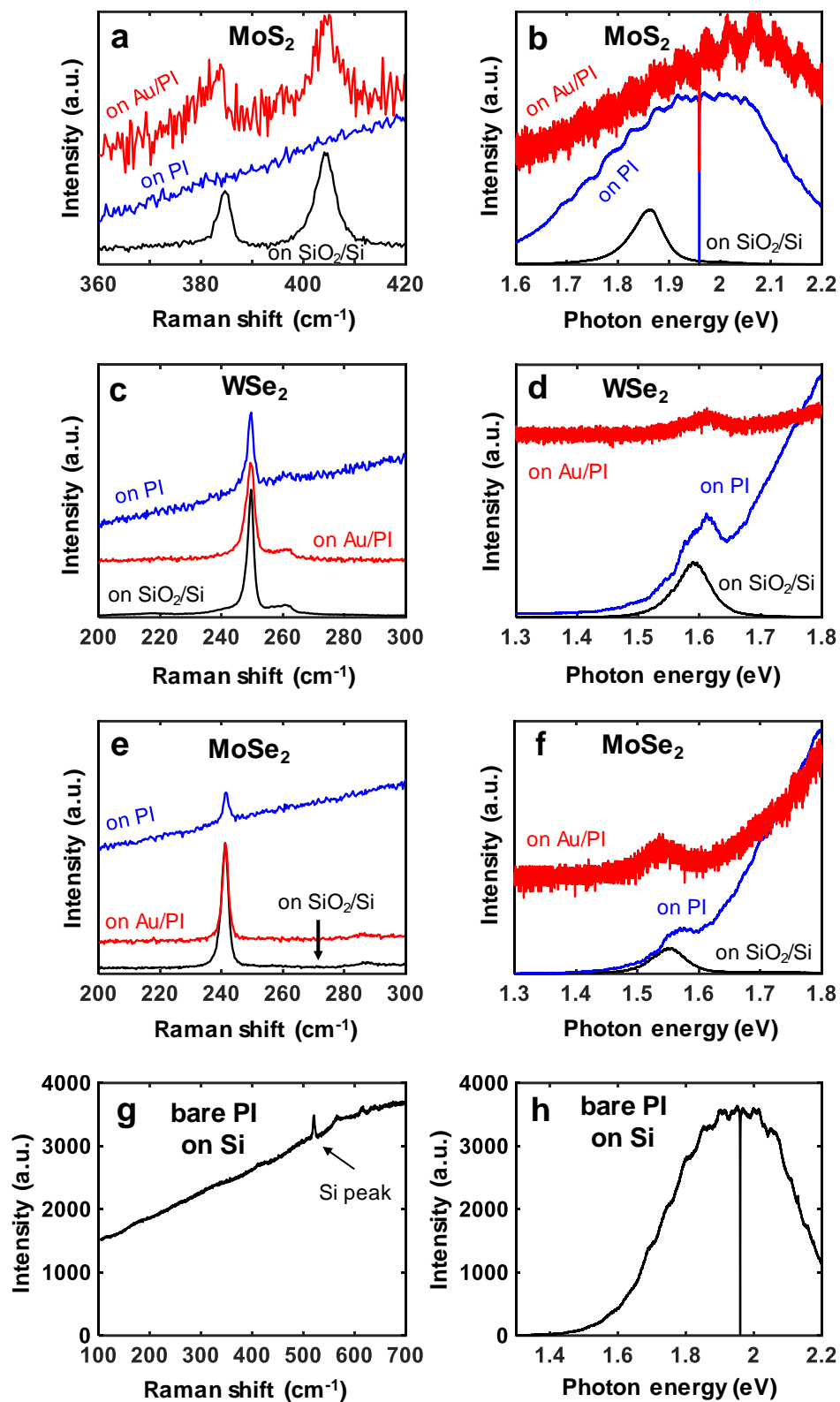
covers and embeds the contacts. After releasing the PI together with metals and TMDs from the SiO₂/Si substrates (main text Fig. 1b), the substrate is flipped over as visible in the numbering (“10”) when comparing Supplementary Fig. S1a,b. This also leads to a reversal of the material stack, where the TMDs are on top of Au/PI or PI, as visible in Supplementary Fig. S1b,d.

B. Raman spectroscopy and Photoluminescence measurements before and after transfer process

The different TMDs were monitored with Raman spectroscopy and photoluminescence (PL) throughout the transfer process to investigate any changes in material properties. Supplementary Fig. S2a-f display the spectra for MoS₂, WSe₂ and MoSe₂ before and after transfer. Since we have deposited and patterned metal contacts before the transfer, released all materials together, and flipped the flexible PI substrate, we were able to measure the TMDs after transfer on the metal surface and on the PI surface.

We observed that the measurements directly on PI (without a metal in between the TMD and PI) have a broad background signal, which is absent on the SiO₂/Si substrates and on Au surfaces. This background signal is in the range where we expect the vibrational modes of the TMDs, and there is, for instance, a significant overlap with the PL energy maximum of monolayer MoS₂ (Supplementary Fig. S2b). The Raman and PL measurements for bare PI (on Si) are shown in Supplementary Fig. S2g,h for comparison. Because of this background signal, the MoS₂ Raman and PL peaks are buried and not visible in our measurements on PI. However, the peaks of WSe₂ and MoSe₂ on the PI surface can be resolved (Supplementary Fig. S2c-f). Further, the insertion of Au between PI and the TMD suppresses this background signal and enables the detection of the Raman signature of all three TMDs.

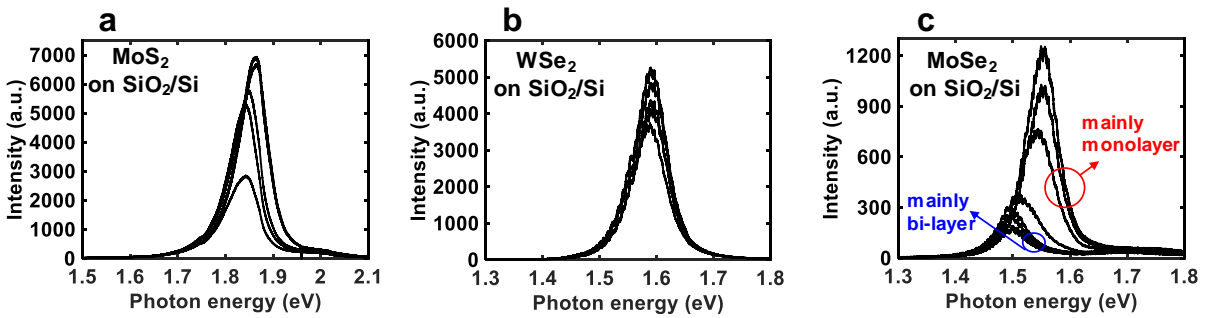
We find that the PL peaks for WSe₂ and MoSe₂ can be detected on PI and Au/PI despite the strong PL quenching that is known to appear on Au surfaces^{30,31}. The PL peak energies of MoS₂, WSe₂ and MoSe₂ are ~1.86 eV, ~1.59 eV and ~1.54 eV, all indicating monolayer thickness^{25,55-57}. While these results were consistent for MoS₂ and WSe₂ across the substrate, we found that MoSe₂ had areas with monolayers and bilayers (~50%) (Supplementary Fig. S3), where the PL peak is shifted towards ~1.50 eV and its intensity is significantly reduced. The noticeable spread in PL energies for MoS₂ can be attributed to a variety of effects such as nanoscale bilayer regions^{23,24} or small local variations in strain or doping. For MoSe₂, however, we find two sets of PL energy peak positions, which indicate that some areas mainly consist of monolayers and some mainly of bilayers (~50% each)^{25,55}.



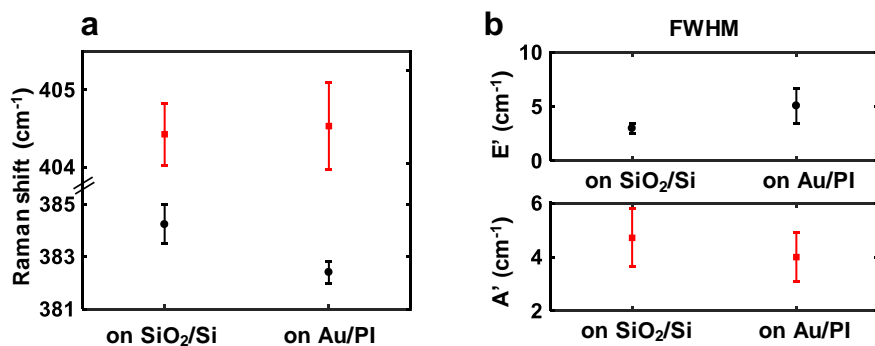
Supplementary Fig. S2 | Raman (left column) and photoluminescence (right column) spectra. a,b, MoS₂. c,d, WSe₂. e,f, MoSe₂. g,h bare polyimide (PI) on silicon.

Changes in the Raman and PL spectra before vs. after transfer can be interpreted as strain release effects or phonon interactions with the bottom surfaces (PI or Au), as will be discussed in the following. For MoS₂ on Au, we find that the E' peak shifts by about -1.8 cm⁻¹ and its full-width-half-maximum (FWHM) increases, whereas the A₁' peak does not change discernably (see Supplementary Fig. S4), which has been observed for non-transferred Au/MoS₂ stacks and thus cannot be correlated with the transfer process. Possible mechanisms for this E' peak shift and broadening can be tensile strain induced from the Au deposition^{58,59} or electron-phonon interactions due to Au plasmons^{60,61}. For WSe₂, the changes in the Raman and PL spectra are small (Supplementary Fig. S5). The minor shifts in the PL peak position and Raman E' peak of about +0.02 eV and -0.1 to -0.2 cm⁻¹, respectively cannot be consistently correlated with any strain release during transfer⁶², and may be related to small effects from interactions with the substrate⁶³. It is difficult to deduce any strain effects from PL and Raman for MoSe₂, due to small changes and existence of mono- and bilayers adding uncertainty to the Raman and PL analysis. Still, the results suggest the possibility of slight strain changes in tensile and compressive directions on Au/PI and PI surfaces, respectively (see Supplementary Fig. S6)⁶⁴⁻⁶⁶.

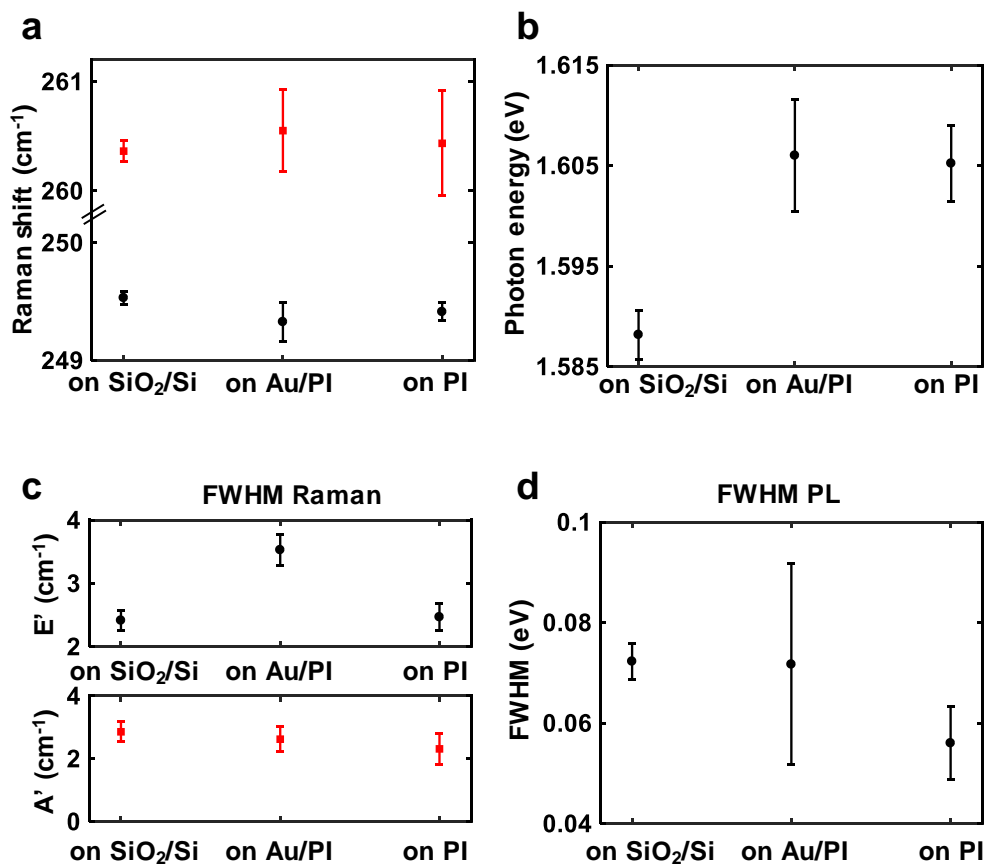
Overall, the FWHM of the Raman and PL peaks for all the TMDs do not increase except on Au electrodes, where previously discussed plasmonic effects could be the leading cause. This indicates that the disorder, which would be affected by crystal grain size or defect density, in the materials is not increased throughout the transfer process^{67,68}. This conclusion is also supported by the good electrical properties, which are comparable on the materials after transfer with those before transfer (i.e. on rigid SiO₂/Si substrates) from previous studies using the same CVD material type^{23,24,69}.



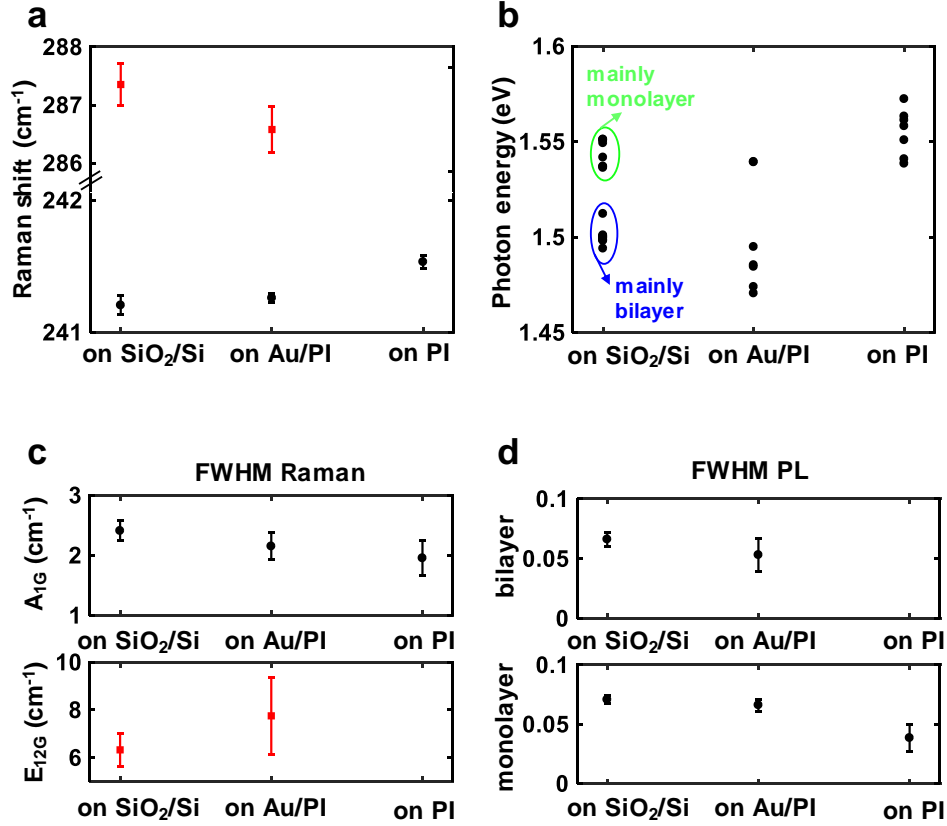
Supplementary Fig. S3 | PL measurements before transfer of **a**, MoS₂, **b**, WSe₂ and **c**, MoSe₂.



Supplementary Fig. S4 | Averaged Raman (over ~5 spots on the same chip) **a**, peak positions and **b**, Full-width-half-maximum (FWHM) of MoS₂ before transfer (as-grown, on SiO₂/Si substrate) and after transfer (on Au/PI).



Supplementary Fig. S5 | Averaged (over ~5 spots on the same chip) **a**, Raman and **b**, photoluminescence (PL) peak positions of WSe₂ before and after transfer. Averaged full-width-half-maximum (FWHM) for **c**, the Raman and **d**, the PL measurements.



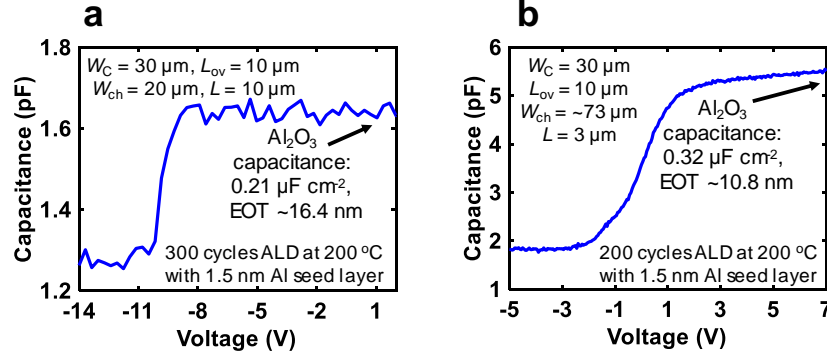
Supplementary Fig. S6 | **a**, Averaged Raman (over ~5 spots on the same chip) and **b**, photoluminescence (PL) peak positions of MoSe₂ before and after transfer. Averaged full-width-half-maximum (FWHM) for **c**, the Raman and **d**, the PL measurements (~10 spots across two chips). Note, missing data e.g., for the Raman E_{12G} peak on PI means that these peaks could not be detected on that particular surface.

C. Mobility, Gate Capacitance, and Threshold Voltage Extraction

We performed the extraction of the extrinsic field-effect mobility $\mu_{FE,ext}$ and threshold voltage V_T from the g_m maximum based on the following equation (valid for small drain-source voltages V_{DS}):

$$g_m = \frac{\partial I_D}{\partial V_{GS}} = \frac{\mu_{FE,ext} C_{ox} V_{DS} W}{L},$$

where the I_D plotted vs. V_{GS} can be fitted linearly to obtain $\mu_{FE,ext}$. Furthermore,^{70,71} the intercept with the V_{GS} axis yields V_T . The channel width W and the channel length L are given by the device geometry. The gate oxide capacitance per unit area (C_{ox}) is determined by connecting source and drain of the transistors to ground, and applying a voltage to the gate electrode. We then perform small-signal capacitance-voltage (C - V) measurements where the direct-current (dc) voltage is swept while applying an alternating-current (ac) voltage with an amplitude = 100 mV and frequency = 20 kHz. The results



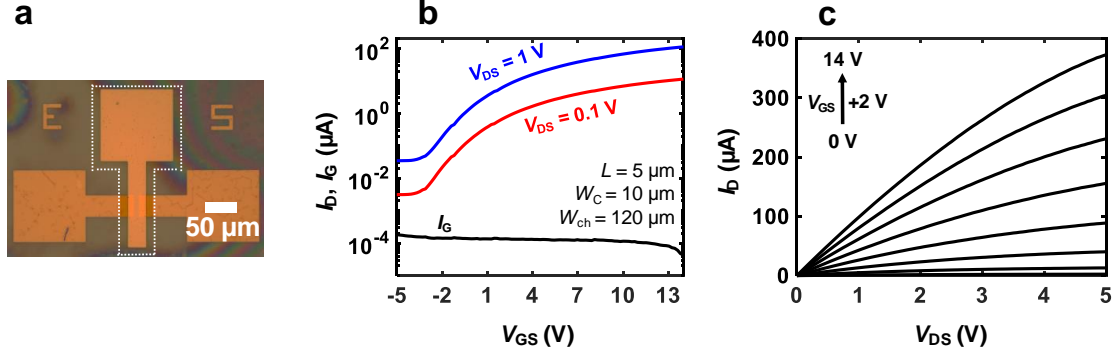
Supplementary Fig. S7 | Measured capacitance-voltage (C-V) characteristics of flexible TMD-FETs. Typical C-V for **a**, MoS₂ FETs and **b**, MoSe₂ and WSe₂ FETs, where the calculated Al₂O₃ capacitance density and equivalent oxide thickness (EOT) represent average values (~5 devices). L_{ov} is the overlap length between the gate electrode and the source/drain electrodes.

for Al₂O₃ gate dielectrics (including 1.5 nm Al seed layer) deposited in 300 cycles (MoS₂ FETs) and 200 cycles (WSe₂ and MoSe₂ FETs) are shown in Supplementary Fig. S7a and Fig. S7b, respectively.

As all transistors are *n*-channel devices, we estimate the capacitance of the Al₂O₃ gate dielectrics at positive bias voltage (when the channel is in accumulation) by dividing the measured capacitance (Supplementary Fig. S7) with the overlap area of the gate with the source, drain, and semiconductor channel³². For MoS₂ FETs the extracted $C_{ox} \approx 0.21 \mu\text{F cm}^{-2}$ or an equivalent oxide thickness (EOT) ~ 16.4 nm, and for WSe₂ and MoSe₂ FETs we obtain $C_{ox} \approx 0.32 \mu\text{F cm}^{-2}$ or EOT ~ 10.8 nm. Estimating the relative dielectric constant ϵ_r from C_{ox} and the Al₂O₃ thickness obtained by ellipsometry, we find $\epsilon_r \approx 7$ -8, which is in the expected range^{72,73}. Note, the ellipsometric thickness of 200 cycles and 300 cycles of atomic-layer deposited (200°C) Al₂O₃ measured on silicon is around 22 nm and 35 nm, respectively. However, for the transistor capacitance the 1.5 nm oxidized Al seed layer adds to the overall thickness, while the optical lithography and lift-off process of the top (gate) electrode exposes the Al₂O₃ to the basic photoresist developer which can etch the material, thus slightly reducing its thickness.

D. Flexible MoS₂ Field-Effect Transistors of Type A

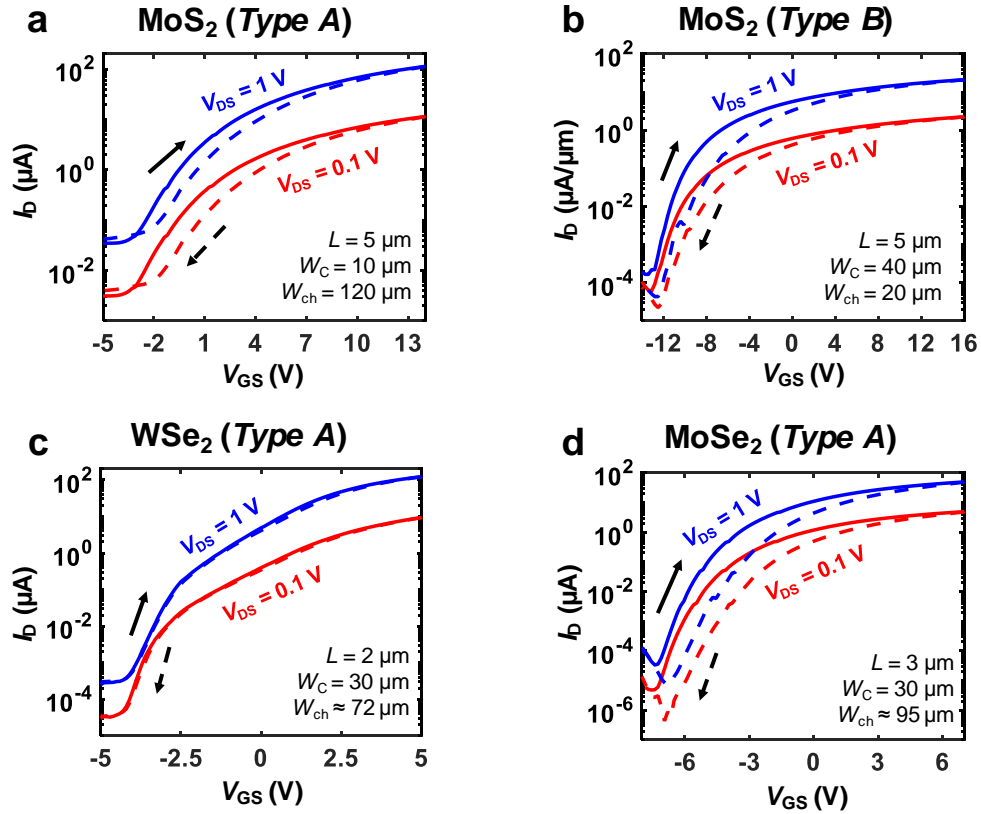
Supplementary Fig. S8 displays a top-down optical microscope image and the electrical characteristics of a flexible MoS₂ field-effect transistor (FET) of *Type A* with 5 μm channel length. The device exhibits an extrinsic field-effect mobility $\mu_{FE,ext} \sim 15 \text{ cm}^2\text{V}^{-1}\text{s}^{-1}$, on-current $I_D \sim 5.4 \mu\text{A } \mu\text{m}^{-1}$ at a drain-source voltage $V_{DS} = 1$ V, threshold voltage $V_T = 3.9$ V, minimum subthreshold swing $SS = \sim 1.7 \text{ V decade}^{-1}$ and on/off ratio $\sim 3.6 \times 10^3$. Note that $\mu_{FE,ext}$ and I_D have been corrected for current spreading, which is described in Section K below.



Supplementary Fig. S8 | MoS₂ field-effect transistors (FETs) of Type A. **a**, Top-down optical microscope image. **b**, Measured transfer characteristics. **c**, Output characteristics.

E. Hysteresis

Comparing hysteresis³³ for *Type A* and *Type B* devices, we find similar maximum values of ~ 1.2 V for MoS₂ FETs, which indicates that the additional etch step before transfer does not deteriorate the TMD interfaces (Supplementary Fig. S9a,b). The WSe₂ FET displays low hysteresis ~ 0.1 V (Supplementary Fig. S9c), and the MoSe₂ FET has a maximum hysteresis of about 1.6 V (Supplementary Fig. S9d).



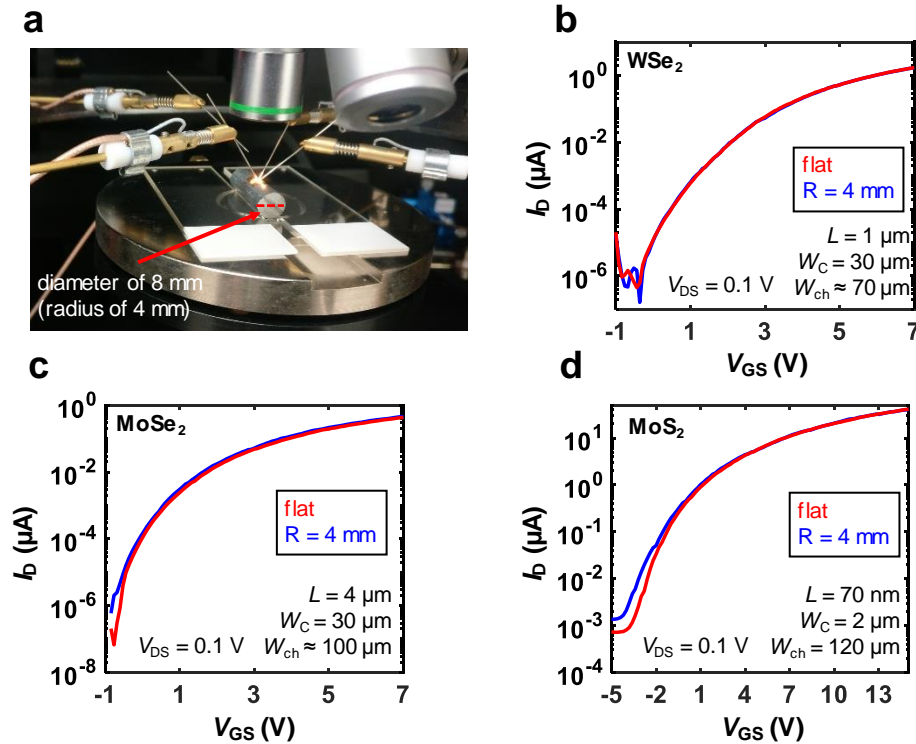
Supplementary Fig. S9 | Hysteresis in flexible transition metal dichalcogenide field-effect transistors. **a**, MoS₂ (*Type A*). **b**, MoS₂ (*Type B*). **c**, WSe₂ (*Type A*). **d**, MoSe₂ (*Type A*).

F. Bending of flexible TMD FETs

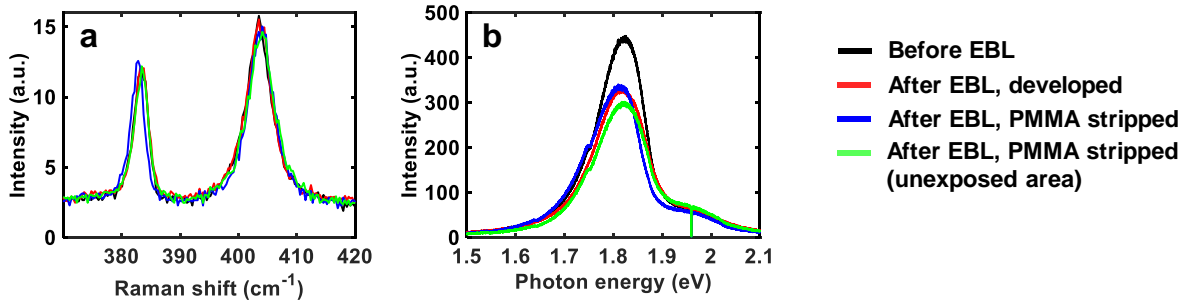
Flexible electronics need to remain unaltered when mechanically deformed, for instance, by bending the substrate. While the ductility of materials matter for the maximum strain that flexible electronics can sustain⁷⁴, the easiest way to minimize impacts of strain on flexible electronic devices is to minimize the substrate thickness. The strain at a given bending radius can be approximated as⁷⁵:

$$strain = \frac{d}{2r},$$

where d is the substrate thickness and r is the radius of curvature. Thus, by minimizing d to a few micrometers, the strain at common bending radii on the order of millimeters is minimized. We show this by using a $\sim 5 \mu\text{m}$ thick PI substrate and bending it to a radius of 4 mm, which results in $\sim 0.063\%$ of strain. Consequently, the electrical characteristics of the TMD FETs remain unaltered in this condition as shown in Supplementary Fig. S10.



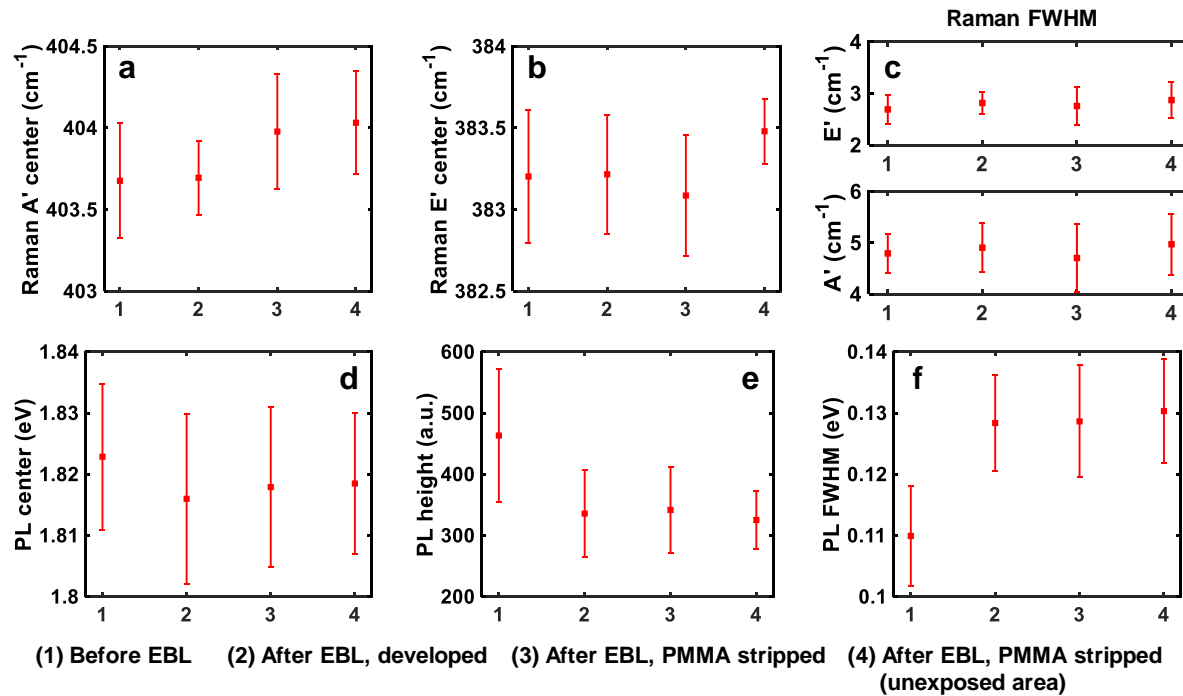
Supplementary Fig. S10 | Mechanical bending of flexible TMD-FETs. **a**, Photograph of the measurement setup where the FETs are bent to a tensile radius of 4 mm. Measured transfer characteristics of **b**, WSe₂ (Type A), **c**, MoSe₂ (Type A) and **d**, MoS₂ (Type A). All show effectively no dependence on substrate bending at the 4 mm radius.



Supplementary Fig. S11 | Optical material analysis of MoS₂ throughout an electron-beam lithography (EBL) process involving spin-coating and stripping of poly(methyl methacrylate) (PMMA). a, Raman spectra. b, Photoluminescence spectra.

G. Electron Beam Lithography on top of MoS₂

Previous reports have indicated that MoS₂ could be damaged by highly energetic electron beams which cause strain and defect formation⁷⁶⁻⁷⁹. We investigated this for our EBL process (details in the Methods section) performing Raman and PL measurements before and after the electron beam exposure and development of the poly(methyl methacrylate) (PMMA) layer that was used for the lift-off of the later



Supplementary Fig. S12 | Averaged optical material analysis of MoS₂ during electron-beam lithography (EBL) with spin-coating and stripping of poly(methyl methacrylate) (PMMA). a, Raman A' peak center. b, Raman E' peak center. c, Averaged full-width-half-maximum (FWHM) of the Raman peaks. d, Photoluminescence (PL) peak center. e, PL peak height. f, PL FWHM.

deposited source/drain metal. Supplementary Fig. S11 displays exemplary Raman and PL spectra, while Supplementary Fig. S12 provides the analysis (averages over 8 spots) of Raman and PL peak center shifts as well as the changes in the intensity and FWHM of the PL spectra. We found negligible differences in the Raman spectra. The slight reduction in the PL intensity (Supplementary Fig. S12) occurs independently of the exposure to the electron beam, and may be caused by PMMA residues or minor effects from processing and aging of the material. Thus, we conclude that here we do not cause significant damage during the EBL process, which may have been due to our 200 nm thick high molecular weight (950K) PMMA layer on top that should reduce the impact energy and dosage of electrons that hit the MoS₂. The other parameters of our EBL process and the device fabrication can be found in the Methods section.

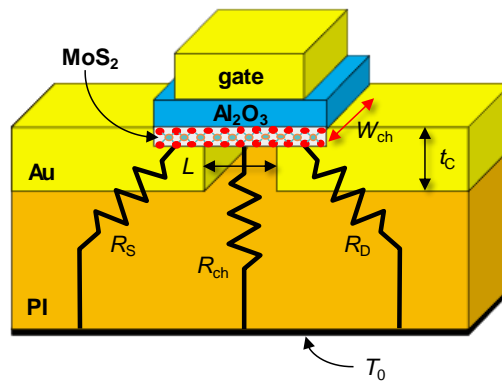
H. Temperature Rise Estimates

We estimate the MoS₂ channel temperature rise in our nanoscale *Type B* devices ($W_{\text{ch}} < W_{\text{C}}$) using the thermal model in Supplementary Fig. S13 below. The heat sink at $T_0 \approx 20^\circ\text{C}$ is below the PI film during measurements, and the PI film thickness is $\sim 5 \mu\text{m}$, larger than any device dimensions here. Three parallel thermal resistance pathways are of importance⁸⁰, direct heat spreading from the channel itself,

$$R_{\text{ch}} \approx \frac{1}{4k_{\text{PI}}(LW_{\text{ch}})^{1/2}}$$

and heat spreading by the Au contacts, $R_{\text{S}} = R_{\text{D}} \approx L_{\text{H}}/(k_{\text{C}}t_{\text{C}}W_{\text{ch}})$ where the thermal healing length

$$L_{\text{H}} \approx \left(\frac{k_{\text{C}}}{4k_{\text{PI}}} t_{\text{C}} \sqrt{W_{\text{ch}}} \right)^{2/3}.$$

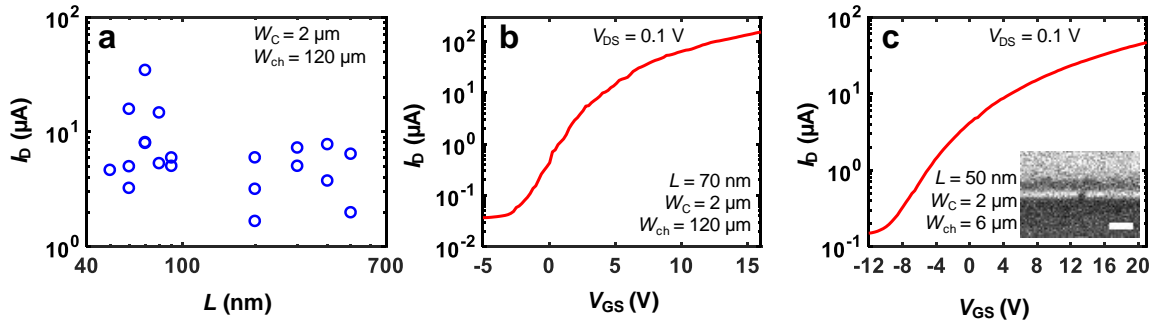


Supplementary Fig. S13 | Thermal model for estimating the channel peak temperature. There are three parallel thermal resistance paths from source (R_{S}), drain (R_{D}) and the channel (R_{ch}) to the heat sink on the bottom of polyimide (PI) with a temperature of $T_0 = 20^\circ\text{C}$. W_{ch} , L and t_{C} represent the channel width, channel length, and Au contact thickness.

The peak temperature rise is estimated as $\Delta T \approx P'W_{ch}(1/R_{ch} + 2/R_S)^{-1}$, where $P' = 420 \text{ W/m}$ is the maximum power input achieved in Fig. 3c, and the relevant dimensions are $L = 100 \text{ nm}$, $W_{ch} = 2 \text{ }\mu\text{m}$, $t_C = 45 \text{ nm}$. We take the thermal conductivity of the thin Au contact $k_C \approx 150 \text{ Wm}^{-1}\text{K}^{-1}$, approximately $2\times$ lower⁸¹ than that of bulk Au and the thermal conductivity of PI at elevated temperatures ($\geq 100^\circ\text{C}$)⁸² as $k_{PI} \approx 0.2 \text{ Wm}^{-1}\text{K}^{-1}$. With these assumptions, we estimate $\Delta T \approx 152 \text{ K}$ or an operating temperature around 172°C , which is $>90\%$ dominated by heat spreading through the source/drain electrodes. This temperature may be slightly overestimated, because heat spreading through the top gate electrode was ignored. However, the thermal boundary resistances between the various materials have also been ignored in this simple model. From the manufacturer process guide⁸³, we note the PI glass transition temperature is 360°C and the decomposition temperature is 620°C . Thus, these devices have additional headroom to operate at higher power, thanks to heat spreading through their source/drain electrodes.

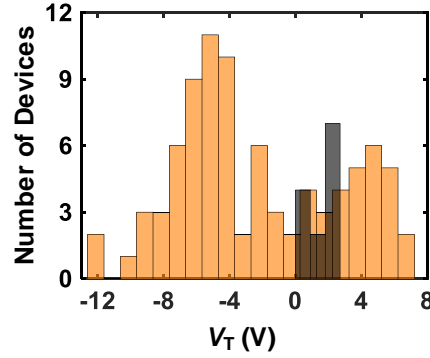
I. Additional *Type A* Device Data and Overall Variability

The variability of I_D for *Type A* devices shows a similar distribution like devices of *Type B* (compare Supplementary Fig. S14a with Fig. 3d). The transfer characteristic of the device with the highest on-current ($L = 70 \text{ nm}$, from Fig. 3f) is displayed in Supplementary Fig. S14b. The shortest channel lengths which we realized were 50 nm and an exemplary electrical characteristic and scanning-electron microscopy cross-section are shown in Supplementary Fig. S14c.



Supplementary Fig. S14 | MoS₂ *Type A* transistors. **a**, Drain current I_D vs. channel length at a drain-source voltage $V_{DS} = 0.1 \text{ V}$ and an overdrive voltage $V_{GS} - V_T = 8 \text{ V}$. **b**, Measured I_D vs. V_{GS} of the device with the highest on-current (also see Fig. 3f). **c**, Electrical characteristic of a *Type A* flexible MoS₂ field-effect transistor with the shortest channel length of 50 nm . Inset shows a scanning-electron microscopy cross-section of such a 50 nm channel. Scale bar: 200 nm .

In Supplementary Fig. S15 we display the histogram for V_T of all MoS₂ devices measured in this work. Academic fabrication and growth variations are the leading cause for the V_T variability, which could be much improved with industrial process optimization (beyond the scope of this work).



Supplementary Fig. S15 | Threshold voltage (V_T) variability of all flexible MoS₂ FETs. V_T extracted with the linear extrapolation method. Most data are for EOT ~16.4 nm (orange) and some data for EOT ~13.7 nm (black). We measured ~100 *Type A* and *Type B* devices, and the geometry, process flows or channel length did not discernably correlate with any V_T changes.

J. Drain current vs. channel length in flexible MoS₂ FETs and Modeling

The drain current I_D that is obtained when probing a short-channel FET typically has contributions from the channel resistance R_{ch} and contact resistance R_C , which makes the accurate extraction of the intrinsic mobility μ_{FE} difficult. Furthermore, since short-channel devices can be contact-dominated, an estimation of R_C is also important. Taking into account R_{ch} and equal source and drain R_C we can estimate the overall resistance R_{tot} (all normalized by device width W , in units $\Omega \cdot m$) as follows:

$$R_{tot}/W = 2R_C/W + R_{ch}/W.$$

Here, this is applied to *Type B* devices ($W = W_{ch} < W_C$), whereas *Type A* devices need an addition correction for current spreading (Section K below). In the linear transistor operating region (at small V_{DS}), R_{ch} can be approximated as

$$R_{ch} = \frac{V_{DS}}{I_D} W \approx \frac{L}{\mu_{FE} C_{ox} (V_{GS} - V_T)},$$

where I_D , L , μ_{FE} , C_{ox} , V_{GS} and V_T are the drain current, transistor channel length, intrinsic field-effect mobility, dielectric capacitance, gate-source voltage and threshold voltage, respectively. Hence, taking into account R_{tot} when measuring the drain current ($I_{D,meas}$) while applying a voltage between drain and source ($V_{DS,appl}$), we obtain the following expression for $I_{D,meas}$ (normalized by W , unit: $A \cdot m^{-1}$):

$$I_{D,meas} = \frac{V_{DS,appl}}{R_{tot}} = \frac{V_{DS,appl}}{2R_C + \frac{L}{\mu_{FE} C_{ox} (V_{GS} - V_T)}}.$$

Thus, we have an expression for $I_{D,\text{meas}}$ where the denominator has two competing components which limit the maximum $I_{D,\text{meas}}$ that can be obtained. Further, we can find that for ultra-scaled transistors in the limit $L \rightarrow 0$, the maximum $I_{D,\text{meas}}$ is fully limited by R_C . In contrast, at long channel devices (here, $L \geq 10 \mu\text{m}$) the R_C no longer has significant impact and $I_{D,\text{meas}}$ is mainly defined by μ_{FE} , given the electrostatics and carrier concentration are fixed (C_{ox} , V_{GS} and V_T constant).

In the following, we use this model to identify lower and upper bounds for R_C and μ_{FE} based on our experimentally obtained results in flexible MoS₂ FETs with channel lengths ranging from 10 μm down to 50 nm. For that we extract $I_{D,\text{meas}}$ at $V_{DS} = 0.1 \text{ V}$ (Fig. 3d) at an overdrive gate voltage ($V_{ov} = V_{GS} - V_T = 8 \text{ V}$) using a V_T extracted from a linear fit of g_m vs V_{GS} . In addition, our model needs C_{ox} , which in this case is $0.21 \mu\text{F cm}^{-2}$ or EOT $\sim 16.4 \text{ nm}$ (Supplementary Fig. S7a). With that, we can use R_C and μ_{FE} as fitting parameters. We obtain upper bounds for $R_C = 2.4 \text{ k}\Omega \mu\text{m}$ and $\mu_{FE} = 28 \text{ cm}^2\text{V}^{-1}\text{s}^{-1}$ for *Type B* devices. Taking into account also the best *Type A* devices, the upper bounds become $R_C = 0.31 \text{ k}\Omega \mu\text{m}$ and $\mu_{FE} = 29 \text{ cm}^2\text{V}^{-1}\text{s}^{-1}$ indicating a remarkably reduced R_C for the *Type A* device at $L = 70 \text{ nm}$. Furthermore, it becomes evident that at channel lengths of 10 μm the devices are dominated by μ_{FE} as changes in R_C do not significantly impact I_D (dotted blue and solid black lines converge in Fig. 3d). This gives us the opportunity to fix the μ_{FE} range at $L = 10 \mu\text{m}$ and then subsequently fit R_C to the highest data points at the smallest channel lengths, where R_C has a larger impact than μ_{FE} , which gives us an estimate for the best R_C . We performed the fitting at $V_{DS} = 0.1 \text{ V}$ (Fig. 3d) to ensure that the devices are in the linear operating regime. We show in Fig. 3c,f that the devices with the highest I_D display effects of self-heating and velocity saturation even below V_{DS} values that would warrant channel pinch-off, which can be commonly observed for sub-100 nm channel length in MoS₂ FETs^{7,35}. However, this does not impact our model because we only use it at low V_{DS} . The model can also be used to predict the extrinsic field-effect mobility $\mu_{FE,\text{ext}}$. The above equations can be modified to³⁶:

$$\mu_{FE,\text{ext}} = \frac{\mu_{FE}}{1 + \frac{\mu_{FE} C_{ox} (V_{GS} - V_T)^2 R_C}{L}}.$$

We used the same input parameters (R_C and μ_{FE}) for $\mu_{FE,\text{ext}}$ as for our I_D fitting. The result shown in Fig. 3e agrees with our extracted $\mu_{FE,\text{ext}}$ based on the maximum g_m method, confirming our calculations.

K. Correction for Lateral Current Spreading in *Type A* FETs

In all our TMD FETs of *Type A*, where the semiconductor width is greater than the electrode width, fringe currents can contribute non-negligibly to the total measured current depending on a number of

factors including contact width and spacing, contact resistance and semiconductor mobility. In order to provide an accurate extraction and comparison of I_D and $\mu_{FE,ext}$ for *Type A* devices and estimate the fringe current effects, we define a dimensionless correction factor:

$$CF = \frac{I_D}{W I_{D,1D}}$$

where I_D is the total current (in μA), W is width of the contact and semiconductor overlap, and $I_{D,1D}$ is the width-normalized current (in $\mu A \mu m^{-1}$) in a FET with the same electrical parameters (sheet and contact resistances) but a channel geometry without current spreading. For FETs without a well-defined patterned channel, $CF > 1$, reflecting the contribution of fringe currents. In the linear regime of the transistor, given R_C , μ_{FE} and bias voltages; $I_{D,1D}$ can be calculated as $V_{DS} \cdot W^{-1} \cdot R_{tot}^{-1}$, with R_{tot} calculated as defined in the previous section. I_D depends on the device and contact geometry as well: we estimate it using 2D finite element method (FEM) simulations using COMSOL Multiphysics to calculate the current distribution. With CF so obtained, width-normalized corrected currents are then

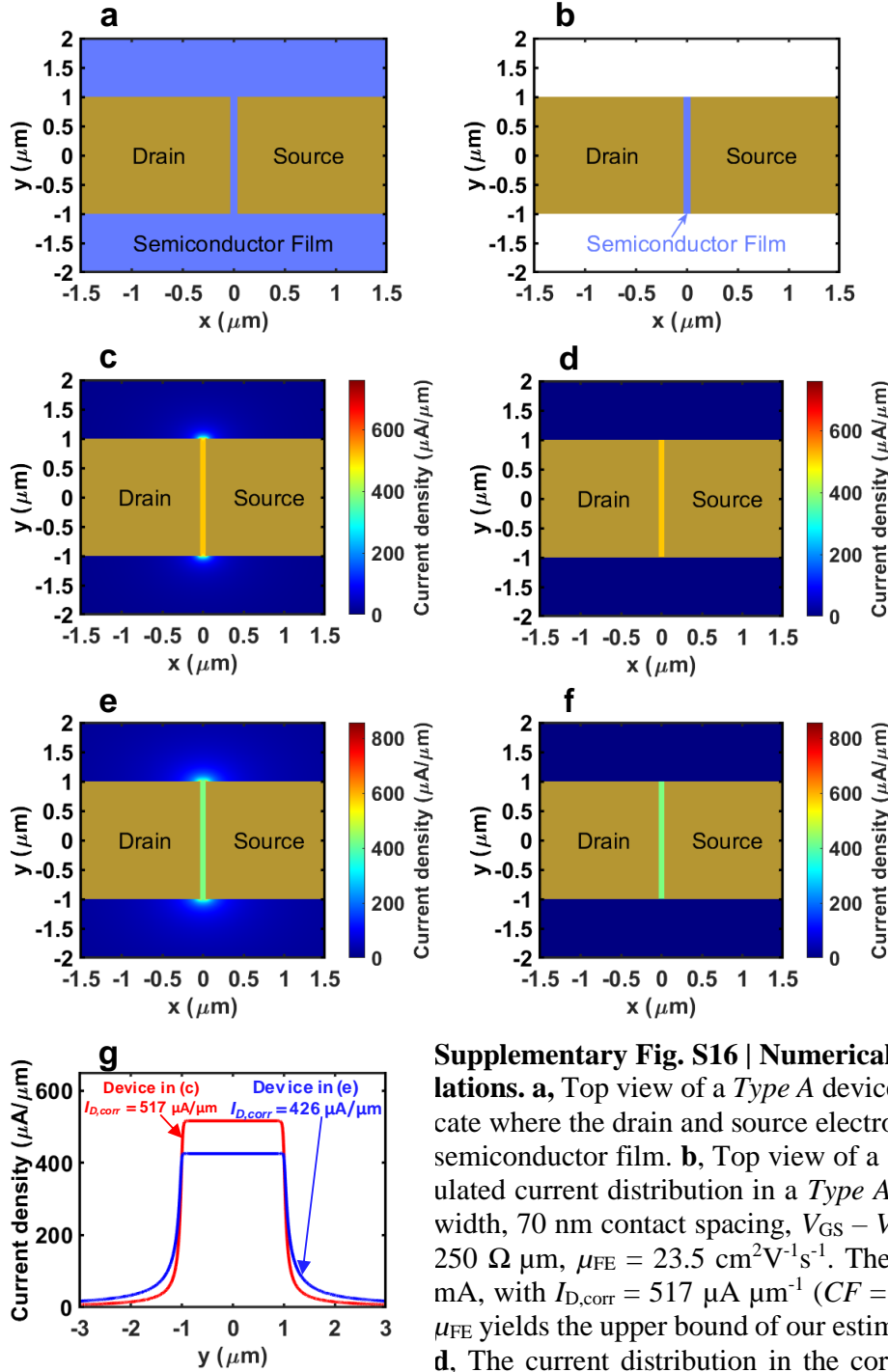
$$I_{D,corr} = \frac{1}{CF} \frac{I_{D,meas}}{W}.$$

In FEM simulations, the transistor is assumed to be in the linear region of operation with $V_{DS} \ll V_{GS} - V_T$, so the semiconductor sheet resistance is assumed to be the same everywhere (except where the semiconductor overlaps with contacts), and given by

$$R_{sh} = \frac{1}{q \mu_{FE} C_{ox} (V_{GS} - V_T)},$$

where q is the elementary electric charge. For purposes of calculating this current distribution, the contacts are assumed to be edge contacts⁸⁴ with a contact resistance per unit width of R_C . The edge contact assumption is equivalent to contacts with current transfer length²⁷ $L_T < 50$ nm.

The two unknown electrical parameters that influence CF are μ_{FE} and R_C . However, for devices without a patterned channel, it is not straightforward to extract these directly from electrical data while simultaneously correcting for fringe currents: a range of CF are possible for different combinations of μ_{FE} and R_C . For the lower end of this range, we assume an $R_C = 250 \Omega \mu m$ (best prior reported results for CVD MoS₂ with Au contacts)²⁴, and fit μ_{FE} to get the measured I_D . For the upper CF estimate, we assume μ_{FE} about 2-fold higher than in our best devices (for CVD MoS₂ a similar value to best prior results on silicon)²⁴ resulting in $\mu_{FE} = 56 \text{ cm}^2 \text{V}^{-1} \text{s}^{-1}$ for MoS₂, $5 \text{ cm}^2 \text{V}^{-1} \text{s}^{-1}$ for MoSe₂ and $10 \text{ cm}^2 \text{V}^{-1} \text{s}^{-1}$ for WSe₂, then fit R_C to get the measured I_D . The range of CF calculated this way yields a range of $I_{D,corr}$ and $\mu_{FE,ext}$, which is illustrated as vertical bars in e.g., Figs. 3d and 3e.



Supplementary Fig. S16 | Numerical current spreading simulations.

a, Top view of a *Type A* device. The regions in gold indicate where the drain and source electrodes are in contact with the semiconductor film. **b**, Top view of a *Type B* device. **c**, The simulated current distribution in a *Type A* device with 2 μm contact width, 70 nm contact spacing, $V_{\text{GS}} - V_{\text{T}} = 10 \text{ V}$, $V_{\text{DS}} = 1 \text{ V}$, $R_{\text{C}} = 250 \Omega \mu\text{m}$, $\mu_{\text{FE}} = 23.5 \text{ cm}^2\text{V}^{-1}\text{s}^{-1}$. The resulting current is 1.225 mA, with $I_{\text{D,corr}} = 517 \mu\text{A} \mu\text{m}^{-1}$ ($CF = 1.186$). This set of R_{C} and μ_{FE} yields the upper bound of our estimated range of $I_{\text{D,corr}}$ values. **d**, The current distribution in the corresponding *Type B* device with the same electrical parameters as in c. The width-normalized current is equal to $I_{\text{D,corr}} = 517 \mu\text{A} \mu\text{m}^{-1}$. **e**, The simulated current distribution in a *Type A* device with 2 μm contact width, at the same bias conditions as in c but with $R_{\text{C}} = 873 \Omega \mu\text{m}$, $\mu_{\text{FE}} = 56 \text{ cm}^2\text{V}^{-1}\text{s}^{-1}$. The resulting current is also 1.225 mA, with $I_{\text{D,corr}} = 426 \mu\text{A} \mu\text{m}^{-1}$ ($CF = 1.438$). This set of R_{C} and μ_{FE} yields the lower bound of our estimated range of $I_{\text{D,corr}}$ values. **f**, The current distribution in the corresponding *Type B* device with the same electrical parameters as in e. The width-normalized current is equal to $I_{\text{D,corr}} = 426 \mu\text{A} \mu\text{m}^{-1}$. **g**, The current density midway between the contacts ($x = 0$) as a function of the y -coordinate. Red and blue curves correspond to the *Type A* devices c and e, respectively.

An example for the current spreading correction is displayed in Supplementary Fig. S16 for a 70 nm long MoS₂ FET. The FEM simulation result displays the current flow paths for two different scenarios of fitted R_C/μ_{FE} (Supplementary Figs. S16c,e). It is visible that the spreading is more pronounced for the scenario with higher μ_{FE} and higher R_C . In Supplementary Figs. S16d and f, the respective I_D distributions with a hypothetical channel width = electrode width are shown which yield $I_{D,1D}$. For this device, we reported in the main manuscript the average values for these two bounds, which is $\sim 470 \mu A \mu m^{-1}$. Finally, Supplementary Fig. S16g displays the current distribution in the y-direction (perpendicular to the channel) at the channel center (defined as $x = 0$), which visualizes the current spreading effect for the two different fitting scenarios.

L. Benchmarking Tables

Reference	Synthesis method	Thickness (nm)	Length (nm)	μ_{FE} or $\mu_{FE,ext}$ ($cm^2 V^{-1} s^{-1}$)	I_D at $V_{DS} = 1V$ ($\mu A \mu m^{-1}$)
Kwon et al. ⁴⁰	exfoliated	30-80	7000	44.8	4.1
Chang et al. ⁴¹	exfoliated	7.9	1000	30*	13
Yoon et al. ⁴²	exfoliated	3.075 (5 layers)	4000	4.7	0.3
Lee et al. ⁴³	exfoliated	1.845 (3 layers)	800	29	NA
Salvatore et al. ⁴	exfoliated	3.5	4300	19	1.3
Yoo et al. ⁴⁴	exfoliated	66.5	8300	83.5	3
Song et al. ⁴⁵	exfoliated	79.3	22600	141.3	1.2
Cheng et al. ¹⁶	exfoliated	1.845 (3 layers)	116	NA	48* ²
Cheng et al. ¹⁶	exfoliated	1.845 (3 layers)	68	NA	135* ³
Ma et al. ⁴⁶	exfoliated	18.3	17500	15.5 \pm 15.9	0.32
Chang et al. ¹⁷	CVD	0.615 (1 layer)	750	31*	66
Amani et al. ⁴⁷	CVD	0.615 (1 layer)	13000	18.9*	0.2
Shinde et al. ²⁹	CVD	0.615 (1 layer)	4000	6.7 \pm 20	2.2
Woo et al. ⁴⁸	CVD	1.538 (2.5 layers)	10000	9	1.4
Park et al. ⁴⁹	CVD	1.23 (2 layers)	4000	17.4	0.13

Supplementary Table S1: Literature values for flexible MoS₂ field-effect transistors used to generate Figs. 4a,b. The synthesis method denotes whether the material was mechanically exfoliated or grown by chemical vapor deposition (CVD). * indicates that in these cases the field-effect mobility μ_{FE} was extracted by the y-function method and contact resistance R_C is excluded. For the other cases the method was either not specified or the transconductance g_m maximum method was used which results in an extrinsic μ_{FE} ($\mu_{FE,ext}$). The drain current I_D is in most cases specified at a drain-source voltage $V_{DS} = 1 V$, unless labeled: *² $V_{DS} = 2V$, *³ V_{DS} not specified.

Reference	Channel material	Length (nm)	on/off ratio	I_D at $V_{DS} = 0.5$ V ($\mu A \mu m^{-1}$)
Park et al. ⁵¹	graphene	140	1.5	248
Yeh et al. ⁵²	graphene	200	8.8	516
Zhai et al. ⁵⁰	single-crystal silicon (c-Si)	150	6×10^7	369
Shahrjerdi et al. ³⁹	single-crystal silicon (c-Si)	30	2×10^5	714
Wang et al. ⁵³	InSnO (ITO)	160	7×10^8	34
Münzenrieder et al. ⁵⁴	InGaZnO (IGZO)	160	7.1	119
Cheng et al. ¹⁶	MoS ₂	116	2×10^6	48*
Cheng et al. ¹⁶	MoS ₂	68	10^6	135* ²

Supplementary Table S2: Literature values for flexible field-effect transistors with channel lengths ≤ 200 nm used to generate Fig. 4c. The drain current I_D is in most cases specified at a drain-source voltage $V_{DS} = 0.5$ V, unless labelled: * $V_{DS} = 2$ V, *² V_{DS} not specified.

Additional References

55. Tonndorf, P. *et al.* Photoluminescence emission and Raman response of monolayer MoS₂, MoSe₂, and WSe₂. *Opt. Express* **21**, 4908-4916 (2013).
56. Liu, B. *et al.* Chemical vapor deposition growth of monolayer WSe₂ with tunable device characteristics and growth mechanism study. *ACS Nano* **9**, 6119-6127 (2015).
57. Plechinger, G. *et al.* A direct comparison of CVD-grown and exfoliated MoS₂ using optical spectroscopy. *Semicond. Sci. Technol.* **29**, 064008 (2014).
58. Gong, C. *et al.* Metal contacts on physical vapor deposited monolayer MoS₂. *ACS Nano* **7**, 11350-11357 (2013).
59. Wang, Y., Cong, C., Qiu, C. & Yu, T. Raman spectroscopy study of lattice vibration and crystallographic orientation of monolayer MoS₂ under uniaxial strain. *Small* **9**, 2857-2861 (2013).
60. Mukherjee, B. *et al.* Exciton emission intensity modulation of monolayer MoS₂ via Au plasmon coupling. *Sci. Rep.* **7**, 41175 (2017).
61. Schauble, K. *et al.* Uncovering the effects of metal contacts on monolayer MoS₂. *arXiv preprint arXiv:2007.14431* (2020).
62. Ahn, G. H. *et al.* Strain-engineered growth of two-dimensional materials. *Nat. Commun.* **8**, 608 (2017).
63. Schneider, L. *et al.* The impact of the substrate material on the optical properties of 2D WSe₂ monolayers. *Semiconductors* **52**, 565-571 (2018).
64. Horzum, S. *et al.* Phonon softening and direct to indirect band gap crossover in strained single-layer MoSe₂. *Phys. Rev. B* **87**, 125415 (2013).
65. Chang, C.-H., Fan, X., Lin, S.-H. & Kuo, J.-L. Orbital analysis of electronic structure and phonon dispersion in MoS₂, MoSe₂, WS₂, and WSe₂ monolayers under strain. *Phys. Rev. B* **88**, 195420 (2013).
66. Ji, J. *et al.* Strain-modulated excitonic gaps in mono- and bi-layer MoSe₂. *Chinese Phys. B* **25**, 077802 (2016).
67. Mignuzzi, S. *et al.* Effect of disorder on Raman scattering of single-layer MoS₂. *Phys. Rev. B* **91**, 195411 (2015).
68. Shi, W. *et al.* Phonon confinement effect in two-dimensional nanocrystallites of monolayer MoS₂ to probe phonon dispersion trends away from brillouin-zone center. *Chinese Phys. Lett.* **33**, 057801 (2016).

69. Somvanshi, D., Ber, E., Bailey, C. S., Pop, E. & Yalon, E. Improved current density and contact resistance in bilayer MoSe₂ field effect transistors by AlO_x capping. *ACS Appl. Mater. Interfaces* **12**, 36355-36361 (2020).
70. Uemura, T. *et al.* On the extraction of charge carrier mobility in high-mobility organic transistors. *Adv. Mater.* **28**, 151-155 (2016).
71. Ortiz-Conde, A. *et al.* A review of recent MOSFET threshold voltage extraction methods. *Microelectron. Reliab.* **42**, 583-596 (2002).
72. Daus, A. *et al.* Ferroelectric-like charge trapping thin-film transistors and their evaluation as memories and synaptic devices. *Adv. Electron. Mater.* **3**, 1700309 (2017).
73. Groner, M., Elam, J., Fabreguette, F. & George, S. M. Electrical characterization of thin Al₂O₃ films grown by atomic layer deposition on silicon and various metal substrates. *Thin Solid Films* **413**, 186-197 (2002).
74. Münzenrieder, N. *et al.* Investigation of gate material ductility enables flexible a-IGZO TFTs bendable to a radius of 1.7 mm. In *2013 Proc. European Solid-State Device Research Conference (ESSDERC)* 362-365 (IEEE, 2013), DOI: 10.1109/ESSDERC.2013.6818893.
75. Lewis, J. Material challenge for flexible organic devices. *Mater. Today* **9**, 38-45 (2006).
76. Matsunaga, M. *et al.* Nanoscale-barrier formation induced by low-dose electron-beam exposure in ultrathin MoS₂ transistors. *ACS Nano* **10**, 9730-9737 (2016).
77. Zan, R. *et al.* Control of radiation damage in MoS₂ by graphene encapsulation. *ACS Nano* **7**, 10167-10174 (2013).
78. Parkin, W. M. *et al.* Raman shifts in electron-irradiated monolayer MoS₂. *ACS Nano* **10**, 4134-4142 (2016).
79. Komsa, H.-P., Kurasch, S., Lehtinen, O., Kaiser, U. & Krashenninnikov, A. V. From point to extended defects in two-dimensional MoS₂: Evolution of atomic structure under electron irradiation. *Phys. Rev. B* **88**, 035301 (2013).
80. Shan, Q., Dai, Q., Chhajed, S., Cho, J. & Schubert, E. F. Analysis of thermal properties of GaInN light-emitting diodes and laser diodes. *J. Appl. Phys.* **108**, 084504 (2010).
81. Lugo, J. & Oliva, A. Thermal properties of metallic films at room conditions by the heating slope. *J. Thermophys. Heat Trans.* **30**, 452-460 (2016).
82. Laumer, T. *et al.* Fundamental investigation of laser beam melting of polymers for additive manufacture. *J. Laser Appl.* **26**, 042003 (2014).
83. *Parameters to make Polyimide Film (PI-2600) with Thickness more than 100 um*, <https://www.researchgate.net/post/Parameters_to_make_Polyimide_Film_PI-2600_with_Thickness_more_than_100_um> (accessed July 28, 2020).
84. Szabó, Á., Jain, A., Parzefall, M., Novotny, L. & Luisier, M. Electron transport through metal/MoS₂ interfaces: edge-or area-dependent process? *Nano Lett.* **19**, 3641-3647 (2019).